



## Security of quantum communications in oceanic turbulence

Zhiyue Zuo, Yijun Wang, Yiyu Mao, Xinchao Ruan , and Ying Guo\*  
*School of Automation, Central South University, Changsha 410083, China*

 (Received 31 August 2021; revised 2 November 2021; accepted 3 November 2021; published 22 November 2021)

The channel fading induced in the ocean quantum links is a major obstacle restricting the performance of ocean quantum key distribution. To determine the ultimate limits at which secret bits (and entanglement) can be distributed via a seawater medium, we propose an analytical model for ocean quantum links to derive the probability distribution of the transmittance, which characterizes the evolution of the quantum state over the fading channel. The proposed model includes the effects of absorption, scattering, turbulence, and ocean thermal noise due to background light. Our comprehensive numerical analysis of several practical scenarios encompasses both pure-loss bounds and thermal-loss bounds, with a submarine at various depths and in various oceans on earth. Besides identifying ultimate limits, we present a security analysis of coherent-state and squeezed-state protocols, showing the secret key rate of both the asymptotic case and finite-size regimes.

DOI: [10.1103/PhysRevA.104.052613](https://doi.org/10.1103/PhysRevA.104.052613)

### I. INTRODUCTION

Quantum key distribution (QKD) exploits the fundamental laws of quantum mechanics to provide a theoretically secure way of sharing secret keys between distant parties, whose basic idea relies on the fact that any attempt to distinguish encoded quantum states causes a disturbance in the signal [1]. To date, QKD has been studied extensively [2] and has become a well-developed technology in real-world applications.

In recent years, the attention towards QKD has increased for a free-space scenario as its ability to provide a global-scale network without the limitation of fiber infrastructure as well as the requirement of a quantum relay. Many works have been carried out for terrestrial [3–5] and satellite-to-ground links [6–8]; however, ocean free-space links are less explored due to the special components and optical properties of seawater. Specifically, the major obstacles in seawater are as follows: (i) The propagation beam is attenuated by the absorption and scattering nature of the medium, including the water's molecular, suspending particles, and even bubbles near the surface [9], and (ii) the beam quality suffers from serious ocean optical turbulence, which is related to the refractive-index fluctuation caused by the random variations of density, salinity, and temperature [10]. Although the fading is harsh compared to fiber and air, the ocean QKD, which acts as the last piece of the puzzle in building a global-scale QKD network, is vital for the secure communication of ocean sensor networks, submarines, and all types of ocean vehicles [11–13]. Unlike traditional ways of applying the acoustic technique, ocean QKD provides unconditional security communication over the seawater medium with high-capacity links and low latency.

Currently, ocean QKDs are underdeveloped from the point of view of both theoretical analysis and experimental verifi-

cation. So far, most underwater experiments are limited to the laboratory using a restricted flume tank [14] or an indoor water pool [13], with no consideration for submarine depth and oceanic turbulence. Ling *et al.*, for example, poured seawater collected from the surface of the coastal sea into a 3.3-m-long glass tube for channel simulation [15]. This channel well maintained the attenuation characteristics of the ocean but had a limited reflection on the impact of depth and temperature variations. For more realistic conditions, Hufnagel *et al.* extended the QKD to an outdoor environment, at the Ottawa River in Canada [16]. The river's varying temperature and currents contributed to natural turbulence conditions; however, this river had a different attenuation and salinity feature than seawater, making the experiment a nondetailed reference for the ocean case. Moreover, Liu *et al.* introduced an alternative scheme [17], based on the spatial light modulator, to simulate the turbulence effects without using the seawater medium. Nevertheless, this method ignored the absorption and scattering factors at the same time. To date, there is still no complete experimental report on ocean QKDs under realistic conditions.

Before the goal of realistic experiments, a reasonable model for ocean quantum links is needed. In fact, the evolution of the quantum state through free space, in terms of the Glauber-Sudarshan  $P$  function [18], can be well characterized by the probability distribution of the transmittance (PDT) due to the negligible depolarization of the free space [19]. In classical-case theory, a well-known technique for PDT description is the log-normal model [20]. Unfortunately, this model is defined in the transmittance range of  $[0, \infty)$ , where the commutation rules for quantum operators would be violated [21]. Peřina *et al.* showed this unphysical artifact on quantum number states caused by the log-normal model in which the attenuating atmosphere creates photons [22]. Recently, Huang *et al.* proposed an underwater entanglement transmission model based on the assumptions of small-angle approximation while the beam deflection distance is treated

\*yingguo@csu.edu.cn

TABLE I. Seawater parameters in various oceans [29].

Ocean type	$c_b$ (mg/m <sup>3</sup> )	( $\times 10^{-3}$ ) $s$ (mg/m <sup>2</sup> )	$h$ (mg)	$d_{\max}$ (m)	$c_{\text{chl}}$ (mg/m <sup>3</sup> )
S1	0.0429	-0.103	11.87	115.4	0.708
S2	0.0805	-0.260	13.89	92.01	1.055
S3	0.0792	-0.280	19.08	82.36	1.485
S4	0.143	-0.539	15.95	65.28	1.326
S5	0.207	-1.03	15.35	46.61	1.557
S6	0.160	-0.705	24.72	33.03	3.323

as the Rice distribution [23]. This model, however, focuses on beam wandering effects and has a simple treatment of the attenuation coefficient and deformation phenomenon. Another promising solution is the so-called phase screen method [24], which can directly simulate the probability distribution using an appropriate turbulence spectrum but requires more calculation steps than the analytical method.

The goal of the present work is to give an analytical method for calculating the PDT of ocean quantum links in a relatively convenient and comprehensive manner. In what follows, we perform a systematic analysis of disturbance effects in horizontal ocean links, including regular losses, optical turbulence, and ocean thermal noises. With the aid of link modeling, we determine the ultimate limits of ocean quantum communications, i.e., the Pirandola-Laurenza-Ottaviani-Banchi (PLOB) bound [25], thermal upper bound, and thermal lower bound, which represent the ultimate converse rates for secret key and entanglement distribution in various ocean and submarine depths. Besides these bounds, we present a security analysis of the squeezed-state protocol [26] that belongs to one of the continuous-variable (CV) QKD protocols.

This paper is organized as follows. In Sec. II we obtain the regular losses between two legal users. We focus on the regular extinction of the optical signal caused by the absorption and scattering of seawater. In Sec. III the statistics of ocean turbulent fields are studied. The power spectrum function allows us to derive the scintillation index, the beam-wandering variance, and the energy redistribution across the beam section based on the elliptical model. In Sec. IV we show the probability parameters of the transmittance that characterizes the evolution of the quantum state in ocean quantum links. Section V provides the ultimate limits and capacities for ocean quantum communications over the horizontal path. An application of the proposed theory on the security analysis of squeezed-state protocols is demonstrated in Sec. VI. Section VII summarizes the paper.

## II. REGULAR LOSSES OF OCEAN LINKS

In this section we focus on the regular losses caused by ocean extinction. By the word “regular” we refer to losses that follow a deterministic manner rather than a random process.

### A. Regular extinction

Ocean extinction, which causes the signal-to-noise ratio to degrade, is associated with molecular absorption and scattering of seawater. In a horizontal link, the overall extinction

losses can be modeled by Beer’s law [27]

$$\eta_{\text{ext}} = e^{-\mathcal{T}z}, \quad (1)$$

where  $\eta_{\text{ext}}$  is the extinction-induced transmittance,  $z$  is the transmission distance, and  $\mathcal{T}$  denotes the seawater extinction coefficient in relation to the wavelength  $\lambda$ , which is given by

$$\mathcal{T} = \mathcal{T}_{\text{abs}} + \mathcal{T}_{\text{sca}}, \quad (2)$$

where  $\mathcal{T}_{\text{abs}}$  is the absorption factor of the ocean and  $\mathcal{T}_{\text{sca}}$  is the scattering factor. In general, the absorption factor is due to the intrinsic absorption of pure water as well as absorption from organic substances, particularly phytoplankton chlorophyll  $a$ . Mathematically, the concentration of chlorophyll  $a$ ,  $c_c(d)$ , varying with the depth  $d$ , follows a Gaussian curve that includes specific seawater parameters and is given by [28]

$$c_c(d) = c_b + sd + \sqrt{2\pi}h\mathcal{J}^{-1}e^{-(d-d_{\max})^2/2\mathcal{J}^2}, \quad (3)$$

where  $c_b$  is the background chlorophyll concentration on the surface,  $s$  is the vertical gradient of concentration,  $h$  is the total chlorophyll above the background levels,  $d_{\max}$  is the depth of the deep chlorophyll maximum, and the standard deviation has the form

$$\mathcal{J} = h[2\pi(c_{\text{chl}} - c_b - sd_{\max})]^{-0.5}, \quad (4)$$

where  $c_{\text{chl}}$  is the maximum chlorophyll concentration at the chlorophyll maximum layer. The seawater parameters of Eqs. (3) and (4) depend on the location of the ocean on earth or, equivalently, the ocean types, as shown in Table I. The scattering factor  $\mathcal{T}_{\text{sca}}$  is related to the scattering by particulate substances and the scattering from pure water, which also depends on  $c_c(d)$ . With the aid of modeling  $c_c(d)$ , the details of  $\mathcal{T}_{\text{abs}}$  and  $\mathcal{T}_{\text{sca}}$  are given in Appendix A.

Figure 1 shows the regular extinction of seawater. In what follows, we focus on two types of oceans: the S1 ocean and the S6 ocean. For fewer losses, the wavelength is set to 532 nm, which is located at the transmission window of seawater (450–550 nm [30]). Figure 1(a) plots the distribution of the extinction coefficient  $\mathcal{T}$  as a function of the depth  $d$ . We find that the extinction coefficient reaches its maximum value at depths of 115 m and 33 m for the S1 and S6 oceans, respectively. Figure 1(b) shows the corresponding extinction-induced transmittance  $\eta_{\text{ext}}$  varying with transmission distance  $z$ . Note that the dashed lines, representing the maximum transmittance at a given distance, are also plotted for comparison. These maximum values are found at a depth of 200 m in both oceans.

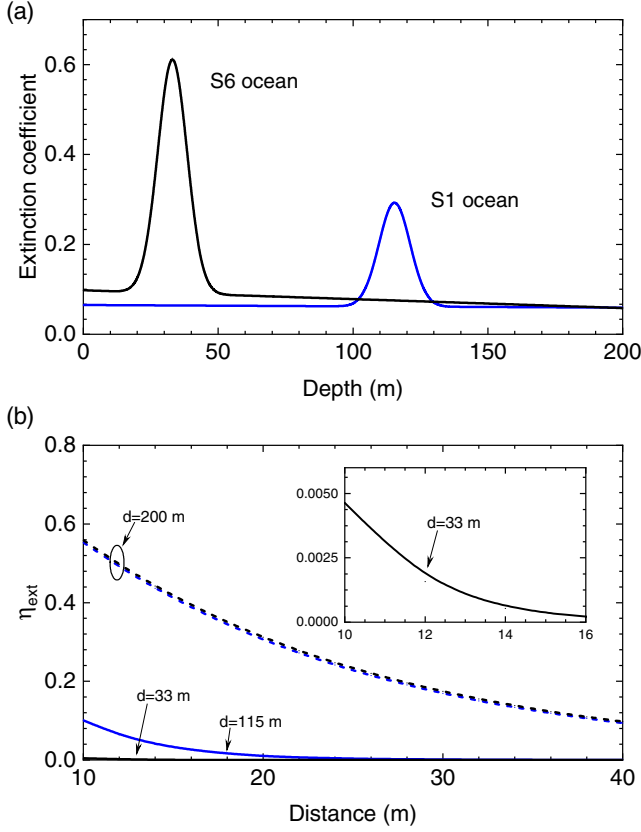


FIG. 1. Regular extinction of seawater for two types of oceans: S1 ocean (blue line) and S6 ocean (black line). (a) Extinction coefficient as a function of submarine depth. The wavelength is set to 532 nm. The other parameters are given in Table I. (b) Extinction-induced transmittance based on Beer’s law varying with transmission distance. The inset shows the 33-m-deep transmittance in the S1 ocean.

### B. Other sources

Besides extinction, both diffraction and device efficiency cause regular losses. The diffraction losses occur due to the receiver telescope, whose circular radius is  $a$ , which may only detect a fraction of the arriving beam since the beam radius will increase from the initial value  $w_0$  to a broadening one  $w_z$  under beam diffraction [31]. Mathematically, the broadening radius is related to the transmission distance and whether the beam is convergent, collimated, or divergent. In what follows, we assume that ocean quantum communication is based on a quasimonochromatic optical mode represented by a collimated Gaussian beam (curvature  $R_0 = \infty$ ). When the collimated beam arrives at the receiver telescope, its radius expands to  $w = w_0[1 + (z/z_{\text{Ray}})^2]^{1/2}$  with the Rayleigh range  $z_{\text{Ray}} = \pi w_0^2/\lambda$ . Finally, the diffraction loss is given by  $\eta_{\text{bro}} = 1 - e^{-2a^2/w_z^2}$  due to the truncation on the finite telescope. However, such broadening seems negligible in the ocean scenario due to its limited transmission distance (usually  $z < 100$  m [20]). Therefore, the diffraction loss is ignored in the following.

Regular losses from device efficiency are dependent on fiber couplings and the detector’s restricted quantum effi-

ciency [32]. To focus on the influence of seawater, we assume an ideal device efficiency, i.e., the device transmittance  $\eta_d = 1$ . Note that the losses caused by regular refraction along the horizontal path are also ignored or, equivalently, the light is assumed to travel in a straight line in nonturbulent seawater.

## III. OCEANIC TURBULENCE

The preceding section ignored the impact of regular refraction, however, other types of refractive phenomena arise in the presence of oceanic turbulence, causing an irregular variation in space and time of the refractive index along the path. In general, this variation is related to the density, salinity, and temperature fluctuations and follows the statistics of turbulent scalar fields [33]. In what follows, we discuss the statistics of turbulent fields and then demonstrate the dependence of beam wandering, beam broadening, and deformation and aperture-averaged scintillations on oceanic turbulence.

### A. Statistical description of oceanic turbulence

The statistical description of oceanic turbulence is based on the so-called energy cascade theory [34]. In general, turbulent seawater motion consists of a family of vortices or eddies of different diameters, bounded above by the outer scale  $L_0$  (macroscale) and below by the inner scale  $l_0$  (microscale). Under the effects of inertial forces, the larger eddies split into smaller eddies to form a continuum of eddy size for the transfer of energy. In the last regime, the seawater eddies die and the remaining energy in the fluid motion is dissipated as heat. Overall, the evolution of seawater eddies causes refractive-index fluctuations along the propagation path, resulting in random variations in light transmittance. In the statistical theory of optical turbulence, the refractive-index fluctuations  $\delta_n$  can be described by the power spectrum

$$\Phi_n(\mathbf{k}) = \frac{1}{(2\pi)^3} \int_{\mathbb{R}^3} d^3\rho \mathcal{B}_n(\rho) e^{-i\mathbf{k}\cdot\rho}, \quad (5)$$

where  $\rho = (x, y, z)^T$  and  $\mathcal{B}_n$  denotes the correlation function given by

$$\mathcal{B}_n(\rho_1 - \rho_2) = \langle \delta_n(\rho_1) \delta_n(\rho_2) \rangle. \quad (6)$$

With the assumption of a locally isotropic and homogeneous random field, the correlation function can be further simplified with Markovian approximation [35] to

$$\begin{aligned} \langle \delta_n(\mathbf{r}; z) \delta_n(\mathbf{r}'; z') \rangle &= 2\pi \delta(z - z') \int_{\mathbb{R}^2} d^2\kappa \Phi_n(\kappa; z) \\ &\times \exp[i\kappa \cdot (\mathbf{r} - \mathbf{r}')], \end{aligned} \quad (7)$$

where  $\mathbf{r} = (x, y)^T$  is the vector of transverse coordinates,  $\kappa = (k_x, k_y)^T$  is the transverse wave vector, and  $\Phi_n(\kappa; z)$  is the simplified turbulence power spectrum. In our work, we apply the classical Kolmogorov power spectrum [36] on oceanic turbulence, which has the form [37]

$$\Phi_n(\kappa; z) = \mathbb{A} \omega(z) \xi^{-1/3}(z) \kappa^{-11/3}, \quad (8)$$

where  $\mathbb{A}$  can be assumed to be of order unity [38],  $\omega(z)$  is related to the dissipation rate of temperature or salinity variance, and  $\xi(z)$  denotes the kinetic energy dissipation rate. With the aid of this ocean power spectrum, the theoretical approach of

free-space quantum light can be used for analyzing the beam evolution of ocean turbulent channels.

### B. Evolution of the quantum state

The evolution theory of the quantum state through the regular lossy and noisy channel is well developed. However, the ocean turbulent channel belongs to the fading channel; therefore the regular tools are not enough. Fortunately, the loss fluctuation or, equivalently, the transmittance fluctuation can be characterized by the PDT function  $\mathcal{P}(\eta)$  due to the seawater transmittance that can be considered as a real random variable [23]. With the aid of  $\mathcal{P}(\eta)$ , the resulting input-output relations of a fading channel, in terms of the Glauber-Sudarshan  $P$  function, can be given by (see the Supplemental Material of Ref. [39])

$$P_{\text{out}}(\alpha) = \int_0^1 d\eta \mathcal{P}(\eta) \frac{1}{\eta} P_{\text{in}}\left(\frac{\alpha}{\sqrt{\eta}}\right), \quad (9)$$

where  $P_{\text{in}}(\alpha)$  and  $P_{\text{out}}(\alpha)$  are the input and output  $P$  functions, respectively. Hence, the evolution of the quantum state over the oceanic turbulence merely reduces to the identification of  $\mathcal{P}(\eta)$ .

To date, there are fewer specific transmittance models for ocean quantum links than there are for the atmosphere [40] due to the more diverse nature of the ocean environment. While atmospheric turbulence is primarily caused by fluctuating temperature, oceanic turbulence is mainly induced by temperature and salinity fluctuations. Therefore, the power spectrum of air is unsuitable for ocean cases and, as consequence, the classical theory cannot be used directly for seawater transmittance. Fortunately, Ref. [33] proposed the mathematical expression for the power spectrum of oceanic turbulence, where the salinity variances can act as refractive blobs distorting the transmitted beam. Following the determination of the power spectrum, numerous papers have been published that upgrade the classical theory by using the ocean power spectrum for the approximate studies on light problems in seawater [37,41]. In this section, the findings developed in previous air research are applied with an upgrade based on the ocean power spectrum in Eq. (8) to reflect the optical conditions of the ocean.

#### Elliptical model

In the present work, we describe  $\mathcal{P}(\eta)$  by the elliptical model [21,42], where the beam profile is assumed to be an elliptic deformation, as depicted in Fig. 2. We assume that a collimated Gaussian beam with an initial radius  $w_0$  is transmitted horizontally onto a telescope, whose aperture radius is  $a$ . In this model, the nonregular losses are caused by the deflection of the beam centroid (beam wandering) and the energy redistribution across the beam section (beam broadening and deformation). These factors can be reflected by the random vector

$$v = (x_0, y_0, \Theta_1, \Theta_2), \quad (10)$$

where  $(x_0, y_0)$  is the beam-centroid coordinate of the arriving beam and  $\Theta_i = \ln(w_i^2/w_0^2)$ , with ellipse semiaxes  $w_i$ , represent the impacts of beam broadening and deformation. With

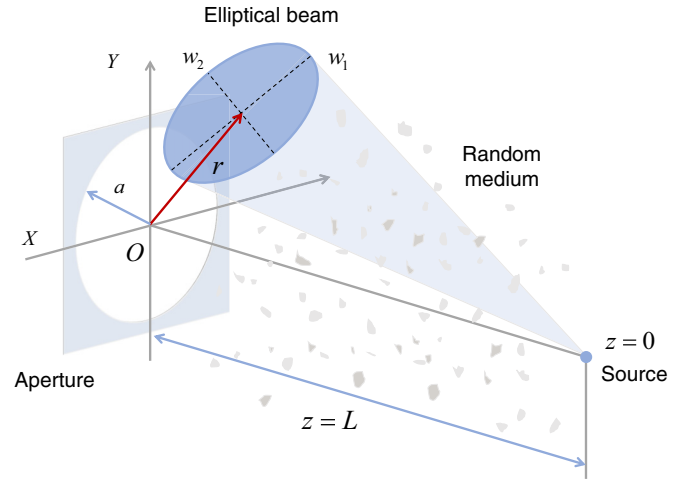


FIG. 2. Elliptical model:  $O$ , beam-centroid position of the receiver telescope;  $w_1$  and  $w_2$ , half axes of the elliptical beam; and  $r$ , beam-centroid vector.

the aid of  $v$ , the total  $\mathcal{P}(\eta)$ , inducing the extinction losses  $\eta_{\text{ext}}$ , can be given by

$$\mathcal{P}(\eta) = \frac{2}{\pi} \int_{\mathbb{R}^4} d^4v \int_0^{\pi/2} d\phi \rho_G(v) \delta(\eta - \eta(v, \phi)), \quad (11)$$

where  $\eta(v, \phi)$  is defined as a function of  $v$  and beam-ellipse orientation angle  $\phi$ . The function  $\rho_G(v)$  is a Gaussian probability density of  $v$  with mean value vector

$$\mathcal{M} = (\langle x_0 \rangle, \langle y_0 \rangle, \langle \Theta_1 \rangle, \langle \Theta_2 \rangle) \quad (12)$$

and covariance matrix

$$\mathcal{C} = \begin{pmatrix} \langle \Delta x_0^2 \rangle & 0 & 0 & 0 \\ 0 & \langle \Delta y_0^2 \rangle & 0 & 0 \\ 0 & 0 & \langle \Delta \Theta_1^2 \rangle & \langle \Delta \Theta_1 \Delta \Theta_2 \rangle \\ 0 & 0 & \langle \Delta \Theta_1 \Delta \Theta_2 \rangle & \langle \Delta \Theta_2^2 \rangle \end{pmatrix}. \quad (13)$$

The derivations of  $\mathcal{M}$  and  $\mathcal{C}$ , based on the ocean power spectrum of Eq. (8) as well as the phase approximation of the Huygens-Kirchhoff method [43], are shown in Appendix B. For horizontal links,  $\omega(z)$  and  $\xi(z)$  are considered as constant at a given depth [41]. In natural seawater,  $\omega$  relates to the dissipation rate of temperature or salinity variances and ranges from  $10^{-2}$  to  $10^{-9} \text{ C}^2 \text{ s}^{-1}$  and  $10^{-2}$  to  $10^{-9} \text{ psu}^2 \text{ s}^{-1}$  (where psu denotes practical salinity unit), respectively;  $\xi$  typically ranges from  $10^{-3}$  to  $10^{-11} \text{ m}^2 \text{ s}^{-3}$ . Since we set a physically allowed interval  $\eta = [0, 1]$  before derivations, the proposed model avoids the deficiency of physical inconsistencies inherent in the log-normal model (defined in the range  $[0, \infty)$ ). With the knowledge of  $\mathcal{M}$  and  $\mathcal{C}$ , we then estimate  $\mathcal{P}(\eta)$  via the Monte Carlo method, as shown in Appendix C. Note that the ocean elliptical model is only suitable for the scenario in which a Gaussian beam is transferred and the random field is locally isotropic and homogeneous.

### IV. PROBABILITY DISTRIBUTION OF TRANSMITTANCE

In this section we investigate the transmittance properties of ocean turbulent channels, including mean transmittance,

TABLE II. Simulation parameters of this work. Here SNU denotes shot-noise units.

Variable	Value	Description	Reference
$z$	10–40 m	Transmission distance (horizontal)	
$d$	0–200 m	Submarine depth	[24]
$\lambda$	532 nm	Wavelength	[30]
$w_0$	80 mm	Initial beam radius	[45]
$a$	0.25 m	Receiver telescope radius	[46]
$\Omega_{\text{fov}}$	522 mrad	Field of view	[46]
$\mathcal{E}$	1440 W/m <sup>2</sup>	Downwelling solar irradiance ( $\lambda = 532$ nm)	[47]
$\mathcal{R}$	1.25%	Underwater reflectance ( $\lambda = 532$ nm)	[47]
$\mu_s$	0.1–1	Squeezed variance	[48]
$\mu_a$	2 SNU	Modulation variance	[7]
$\beta$	95%	Reconciliation efficiency	[49]

variance, and aperture-averaged scintillations. In what follows, we focus on a challenging regime with strong turbulence, i.e.,  $\omega = 10^{-11}$  and  $\xi = 10^{-3}$  (for strong turbulence  $\omega \in [10^{-11}, 10^{-10}]$  and  $\xi \in [10^{-5}, 10^{-3}]$  [37]). The case of weak turbulence can be obtained by updating the values of  $\omega$  and  $\xi$ . Typically, the value of  $\omega\xi^{-1/3}$  in weak turbulence is around  $10^{-14}$  [41]. For the sake of simplicity, we ignore the depth-induced fluctuation of  $\omega$  and  $\xi$  while considering the optimal working condition of  $\langle x_0 \rangle = \langle y_0 \rangle = 0$ . In practice however, one may hold a nonzero average deflection [44], i.e.,  $\langle x_0 \rangle \neq \langle y_0 \rangle \neq 0$ . The simulation parameters are listed in Table II. Note that we set an upper limit of 200 m on the depth since the deeper water is cold and very dense [24].

### A. Mean transmittance and variance

Figure 3 shows the mean transmittance  $\langle \eta \rangle$  and variance  $\text{Var}(\sqrt{\eta})$  vs the transmission distance  $z$  and the depth  $d$  for two types of oceans: the S1 ocean and the S6 ocean. The time of the Monte Carlo method is set to 10 000 for reliable results. In Fig. 3(a) we plot the mean transmittance  $\langle \eta \rangle$  of the S1 ocean. The gray surface, representing the nonturbulence transmittance based on Beer's law [cf. Eq. (1)], is also plotted for comparison. We find that oceanic turbulence increases attenuation and that the mean transmittance is lowest at a depth of 115 m. Figure 3(b) shows the variance  $\text{Var}(\sqrt{\eta}) = \langle \eta \rangle - \langle \sqrt{\eta} \rangle^2$  of the S1 ocean, which is related to the strength of transmittance fluctuations [50]. The gray surface represents the mean value of  $\text{Var}(\sqrt{\eta})$  throughout the simulation region. We find that the S1 ocean belongs to weakly fluctuating quantum channels as the values of  $\text{Var}(\sqrt{\eta})$  are all less than  $10^{-3}$  [51]. For example, the transmittance jitters in the range  $\eta = [0.1216, 0.1710]$  with a standard deviation of 0.0057 when the depth is 200 m and the transmission distance is 15 m. In Figs. 3(c) and 3(b) we plot  $\langle \eta \rangle$  and  $\text{Var}(\sqrt{\eta})$  of the S6 ocean, respectively. We find that the statistics of the S6 ocean differ from those of the S1 ocean. When the ocean is changed from S1 to S6, the depth of the lowest mean transmittance decreases from 115 to 33 m. This result shows the importance of changing the depth in terms of ocean type for a better transmission in use. Moreover, the S6 ocean also belongs to weakly fluctuating quantum channels according to the values of  $\text{Var}(\sqrt{\eta})$ .

### B. Aperture-averaged scintillations

Fluctuations in received irradiance caused by optical turbulence are commonly referred to as scintillation. Physically, the scintillation index is defined as the normalized variance of the irradiance fluctuations [52]. Knowledge of the scintillation index is crucial for determining system performance in a communication system or radar link (see Chaps. 11 and 13 in [34]). Mathematically, the scintillation index is given by

$$\sigma_I^2 = \frac{\langle I^2(\mathbf{r}, z) \rangle}{\langle I(\mathbf{r}, z) \rangle^2} - 1, \quad (14)$$

where  $I(\mathbf{r}, z)$  is the irradiance of light. However, the scintillation index above denotes the physical quantity obtained by a point aperture. In practice, increasing the collecting area of the receiver telescope reduces scintillation, which is known as aperture averaging [52]. In detail, the aperture-averaged scintillation is derived from the ratio of power fluctuations by the telescope collecting area to that obtained by a point aperture, which has the form [53]

$$\sigma_\eta^2 = \frac{\langle \eta^2 \rangle - \langle \eta \rangle^2}{\langle \eta \rangle^2}, \quad (15)$$

where the transmittance

$$\eta = \int_{\mathcal{A}} d^2\mathbf{r} I(\mathbf{r}, z), \quad (16)$$

with the aperture area  $\mathcal{A}$ . Mathematically, the elements in Eq. (15) can be deduced from the field correlation function given by

$$\langle \eta^2 \rangle = \int_{|\mathbf{r}_1| \leq a} d^2\mathbf{r}_1 \int_{|\mathbf{r}_2| \leq a} d^2\mathbf{r}_2 \Gamma_4, \quad (17)$$

$$\langle \eta \rangle = \int_{|\mathbf{r}| \leq a} d^2\mathbf{r} \Gamma_2, \quad (18)$$

with the second-order field correlation function  $\Gamma_2 = \langle I(\mathbf{r}, z) \rangle$  and the fourth-order field correlation function  $\Gamma_4 = \langle I(\mathbf{r}_1, z)I(\mathbf{r}_2, z) \rangle$ . For the derivations of  $\Gamma_2$  and  $\Gamma_4$  refer to Appendix B. In fact, the parameters, which characterize statistical properties of the elliptic model, are expressed in terms of  $\Gamma_2$  and  $\Gamma_4$  [see Eqs. (B5)–(B7)].

Figure 4 shows the aperture-averaged scintillation index  $\sigma_\eta^2$  vs the transmission distance  $z$  with different receiver telescope radii. Without loss of generality, we present the results of the

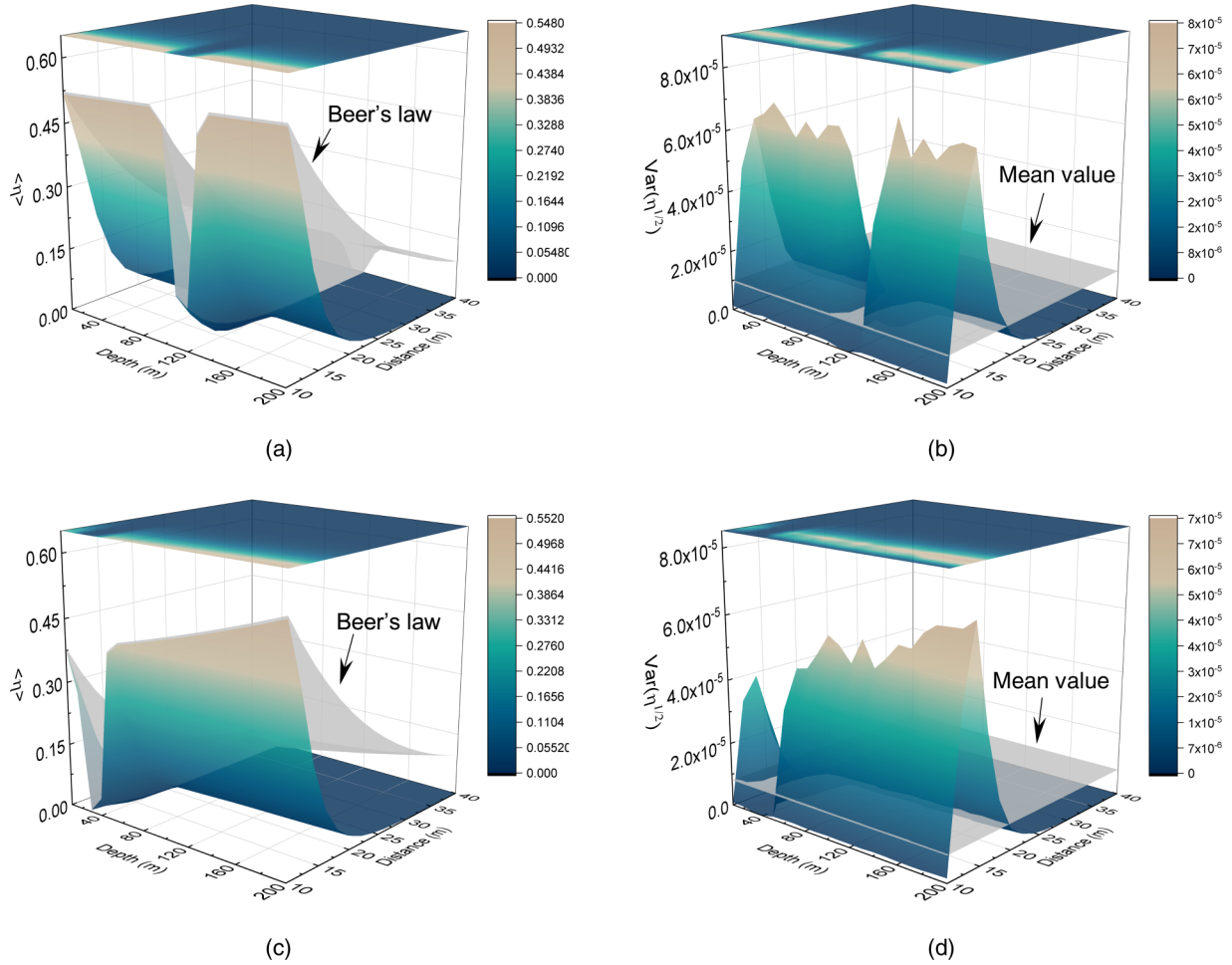


FIG. 3. Statistics of transmittance varying with the transmission distance and the depth for (a) and (b) the S1 ocean and (c) and (d) the S6 ocean. Here the dissipation rate  $\omega = 10^{-11}$  and the kinetic energy dissipation rate  $\xi = 10^{-3}$ . Refer to Table II for the system parameters. The mean values of  $\text{Var}(\sqrt{\eta})$  are (b)  $9.73 \times 10^{-6}$  and (d)  $8.09 \times 10^{-6}$ .

S6 ocean at a depth  $d = 200$  m. This is possible since we ignore the depth-induced fluctuation on  $\omega$  and  $\xi$ . We find that the aperture-averaged scintillation index does not continue to

rise as transmission distance increases. Taking the case of  $a = 0.25$  m as an example, the scintillation index reaches the peak at  $z = 16$  m and then decreases. In addition, the increasing telescope radius (from 0.11 m to 0.25 m) reduces the scintillation index, especially if the transmission distance is less than 20 m. When the transmission distance exceeds 30 m, the line of  $a = 0.25$  m collapses to that of  $a = 0.11$  m, as shown in the inset.

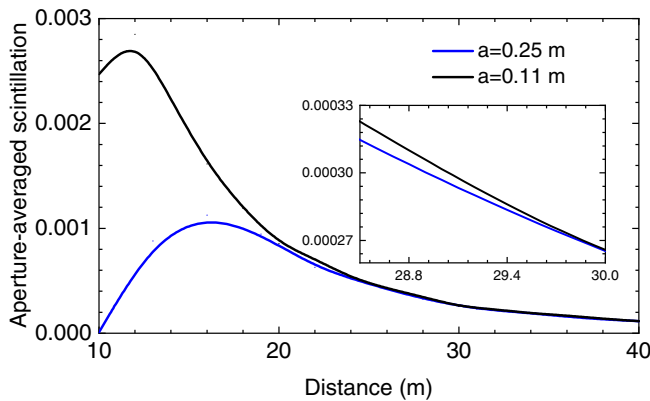


FIG. 4. Aperture-averaged scintillation index vs transmission distance with receiver telescope radii  $a = 0.25$  m (blue line) and  $a = 0.11$  m (black line). The inset shows a close-up from 28.5 to 30 m.

### V. BOUNDS FOR OCEAN QUANTUM COMMUNICATIONS

Once we have identified  $\mathcal{P}(\eta)$ , we can derive the bound of maximum secret bits that are achievable by ocean quantum communications. In general, we determine the secret key capacity and the two-way entanglement distribution capacity of the pure-loss channel by the point-to-point repeaterless PLOB bound [25]. Using the convexity properties of the relative entropy of entanglement [54], the PLOB bound of the fading channel is given by the average [4]

$$\mathcal{K}_{\max} \leq - \int_0^1 d\eta \mathcal{P}(\eta) \log_2(1 - \eta), \quad (19)$$

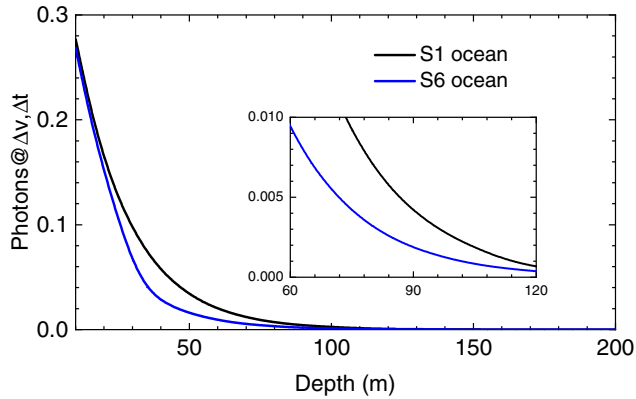


FIG. 5. Background photons vs depth for two types of oceans. The inset shows the background noise from 60 to 120 m.

where  $\mathcal{K}_{\max}$  is the maximum rate of secret key bits that can be distributed per transmitted mode. However, the ocean quantum link is not a pure-loss one but adds thermal noise, such as the background thermal photons coupling into the output mode. Even though such noise is trusted, Eq. (19) is no longer guaranteed to be achievable. In this section, we first show the thermal noise caused by background light and then derive the tighter bounds for thermal-loss ocean quantum links.

#### A. Thermal noise

In the ocean scenario, the background photons from the sun or other stellar objects are dependent upon the depth  $d$ . In general, the deeper ocean is less noisy than the shallow one due to the background photons that will be absorbed by the seawater [55]. Mathematically, the number of background photons landing on the receiver telescope at depth  $d$  can be expressed as [47]

$$\mathcal{N}_{\text{back}} = \tau \Delta_f \frac{\mathcal{L}_{\text{sol}} \Omega_{\text{fov}} \pi a^2 \eta_r \eta_f}{h_0 \nu_w}, \quad (20)$$

where  $h_0$  is Planck's constant,  $\nu_w$  is the frequency of light in water with a water light speed  $2.25 \times 10^8$  m/s,  $\tau$  is the effective sampling period,  $\Delta_f$  is the optical filter bandwidth,  $\Omega_{\text{fov}}$  is the field of view,  $\pi a^2$  denotes the receiver area,  $\eta_r = 1$  is the band filter transmission,  $\eta_f = 0.1881$  is the optical filter transmissivity, and the solar radiance  $\mathcal{L}_{\text{sol}}$  in  $\text{W m}^{-2} \text{sr}^{-1} \mu\text{m}^{-1}$  is given by

$$\mathcal{L}_{\text{sol}} = \pi^{-1} \mathcal{E} \mathcal{R} \mathcal{L}_f e^{-\eta_a d}, \quad (21)$$

where  $\mathcal{E}$  is downwelling irradiance,  $\mathcal{R}$  is the underwater reflectance of downwelling irradiance,  $\mathcal{L}_f$  is the factor describing the directional dependence underwater, which equals 2.9 at a viewing angle of  $\pi/2$  (looking horizontally) [56], and  $\eta_a$  is the average attenuation of the water column from the surface to the communication depth. Finally, the total number of thermal photons, which is related to the device transmittance  $\eta_d$ , is given by

$$\mathcal{N} = \eta_d \mathcal{N}_{\text{back}} + \mathcal{N}_{\text{ex}}, \quad (22)$$

where  $\mathcal{N}_{\text{ex}}$  is the excess photons beside the natural background.

Figure 5 shows the background photons collected by the receiver telescope as a function of the depth  $d$  for two types

of oceans. The simulation parameters are shown in Table II. Here we set the optical filter bandwidth  $\Delta_f$  and the effective sampling period  $\tau$  to 1 nm and 1 ns, respectively [30]. We find that background photons in the S6 water fall faster than in the S1 ocean. Moreover, the background photons of both oceans are reduced to less than  $10^{-2}$  for depths above 75 m. Note that  $\Delta_f = 1$  nm is the value of the narrow-band filter typically considered in works with discrete variables. In the CV scenario, narrower filters are available by using suitable interferometric procedures at Bob's side [4].

#### B. Analysis of the ultimate bounds

In this section we derive the thermal-loss bounds of ocean quantum communication based on the thermal noise discussed above. The total input-output relation of thermal photons from the transmitter to the receiver is equivalent to a beam splitter mixing the signal mode with the input photons of

$$\mathcal{N}_e = \mathcal{N}/(1 - \eta). \quad (23)$$

For the sake of simplicity, we keep  $\mathcal{N}$  constant, regardless of the instantaneous transmittance  $\eta$ . Once we have clarified the input-output relation of thermal noise, we determine the thermal bounds for distributing keys (and entanglement) with ocean quantum links. According to [25], the relative entropy of entanglement suitably computed over the asymptotic Choi matrix of the thermal-loss channel provides an upper bound for its secret key capacity. Then any key rate under a fading channel cannot exceed the thermal upper bound [4]

$$\mathcal{K}_{\max} \leq - \int_{\mathcal{N}}^1 d\eta \mathcal{P}(\eta) [\log_2(1 - \eta) + \mathcal{N}_e \log_2 \eta + \mathcal{H}(\mathcal{N}_e)], \quad (24)$$

where  $\mathcal{H}(x) := (x + 1) \log_2(x + 1) + x \log_2(x)$ . Besides the thermal upper bound, we can derive the thermal lower bound for distributing keys (and entanglement) in terms of the reverse coherent information [57], which has the form

$$\mathcal{K}_{\max} \geq - \int_0^1 d\eta \mathcal{P}(\eta) [\log_2(1 - \eta) + \mathcal{H}(\mathcal{N}_e)]. \quad (25)$$

These formulas allow us to calculate the ultimate rates for key (and entanglement) distributions that are available via a fading channel containing thermal photons. When the thermal photons are negligible, the bounds in Eqs. (24) and (25) collapse to the bound in Eq. (19).

Figure 6 shows the ultimate bounds vs the transmission distance  $z$  for two types of oceans. Here we consider the optimal case with an ideal lossless and noiseless receiver, i.e.,  $\eta_d = 1$ , and  $\mathcal{N}_{\text{ex}} = 0$ . This can be applied to bound the protocols where both local noise and the limited efficiency of the detector are regarded as trustworthy. Figure 6(a) shows the ultimate bounds of the S1 ocean at different depths. At a depth of 100 m, we find that the thermal upper bound is close to the thermal lower bound in the short-distance case, but there is a clear gap between the two thermal bounds if the transmission distance exceeds 18 m. This is because the background photons  $\mathcal{N}_{\text{back}}$ , as shown in the inset table, are limited at the 100 m depth, causing a negligible gap between two thermal bounds in the short-distance case. When the transmission distance increases or, equivalently, the transmittance decreases,

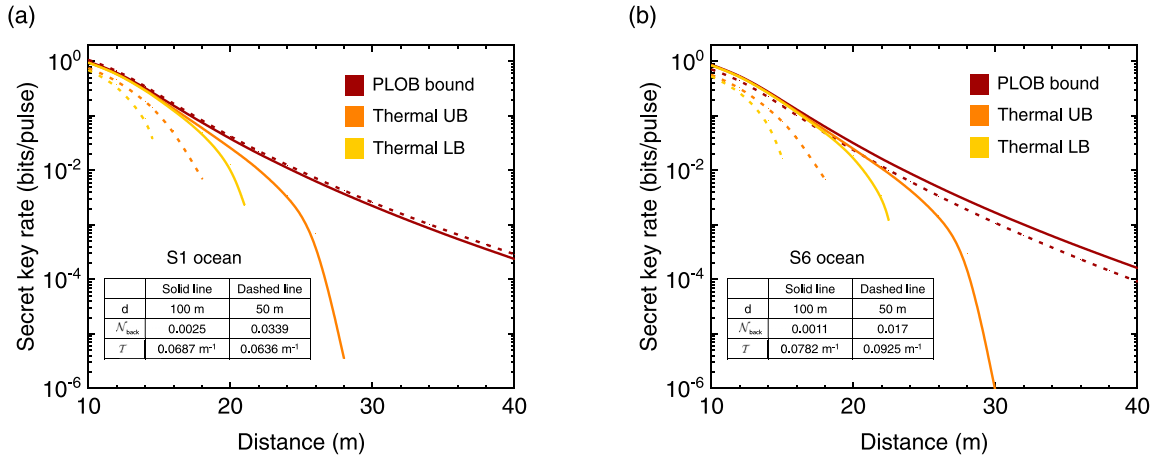


FIG. 6. Ultimate bounds vs the transmission distance for (a) the S1 ocean and (b) the S6 ocean. The depth is set to 50 m (dashed line) and 100 m (solid line) as examples. The inset table shows the channel parameters of each depth. Here UB denotes upper bound and LB lower bound.

the equivalent thermal noise  $\mathcal{N}_e$  goes up [cf. Eq. (23)] and thus the gap between two thermal bounds appears. In contrast, the gap between two thermal bounds always exists at a 50 m depth because the background photons at 50 m depth are one order of magnitude larger than at 100 m depth. An interesting observation is that the PLOB bound at the 50 m depth is higher than the one at the 100 m depth; however, the two thermal bounds at the 100 m depth are wider than those at the 50 m depth. This is because the PLOB bound is a pure-loss bound that does not rely on thermal noise. The light at the 50 m depth has a more favorable transmittance than light at the 100 m depth (see the extinction coefficient  $\mathcal{T}$  in the inset table); thus the PLOB bound is higher at the 50 m depth. Figure 6(b) shows the ultimate bounds of the S6 ocean at different depths  $d$ . We find that the three bounds are higher at the 100 m depth than at the 50 m depth. Similarly, at the 100 m depth, the gap between the thermal upper bound and the thermal lower bound appears only when the transmission distance exceeds 20 m. However, this gap always exists if Alice and Bob raise the depth from 100 m to 50 m.

### VI. APPLICATION: SQUEEZED-STATE PROTOCOL

In this section we use the proposed theory of ocean quantum links to calculate the secret key rate when using the squeezed-state protocol. We first discuss the notion of the squeezed-state protocol and then account for the secret key rate in both the asymptotic case and the finite-size regimes. To be consistent with the preceding analysis, we consider the case of an ideal lossless and noiseless receiver (i.e.,  $\eta_d = 1$  and  $\mathcal{N}_{\text{ex}} = 0$ ). For the system parameters refer to Table II. Note that the minimum squeezed variance is limited to  $\mu_s = 0.1$ , which has been obtained experimentally [48].

#### A. Description of the protocol

The prepare-and-measure schematic of the squeezed-state protocol over the ocean turbulent channel is shown in Fig. 7. It can be described as follows.

*Step 1: State preparation.* The sender Alice randomly generates  $X$  or  $P$  quadrature-squeezed vacuum states by using the optical parametric oscillator (OPO). Without a loss of

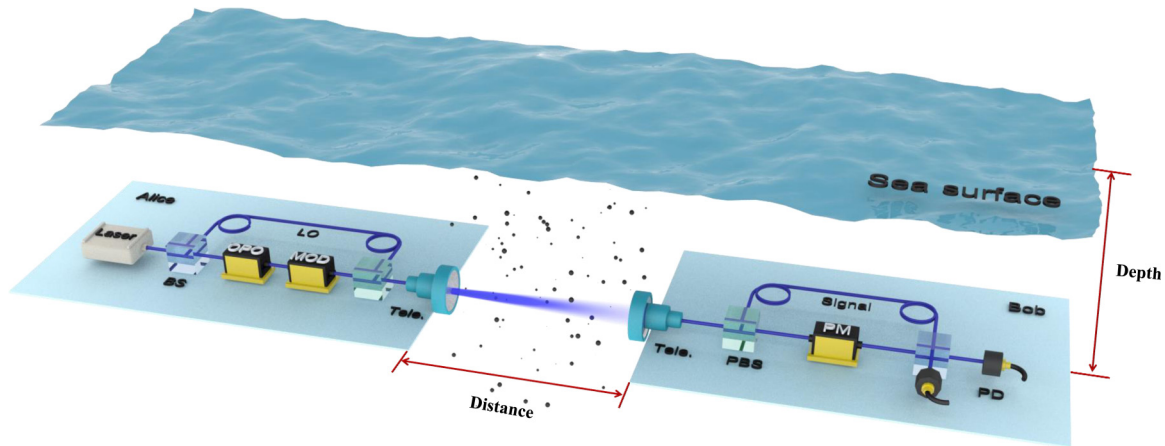


FIG. 7. Schematic diagram of the squeezed-state protocol over the ocean turbulent channel: OPO, optical parametric oscillator; MOD, modulator; BS, beam splitter; LO, local oscillator; PBS, polarization beam splitter; Tele., telescope; PM, phase modulator; and PD, photodetector.



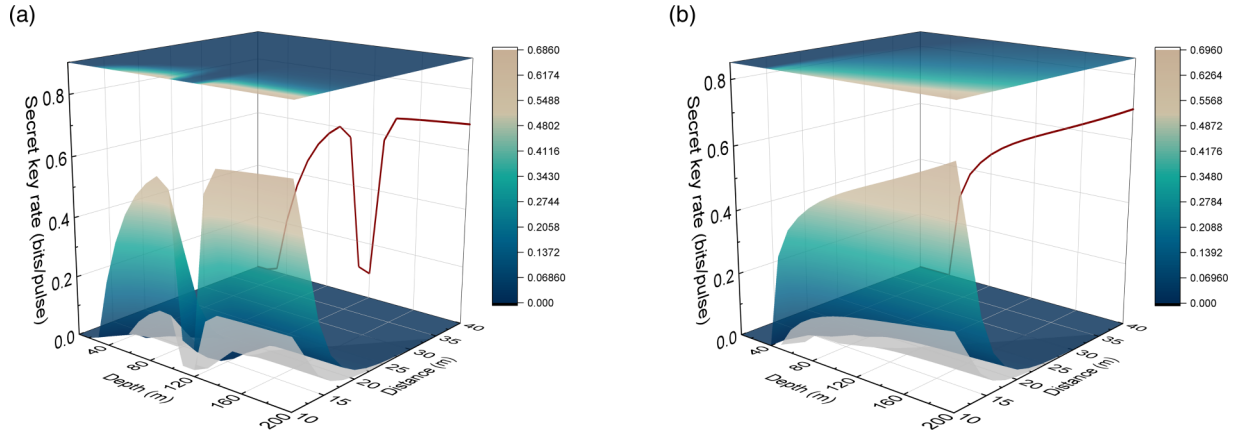


FIG. 8. Asymptotic key rates of the squeezed-state protocol in (a) the S1 ocean and (b) the S6 ocean. The gray surface represents the secret key rates of the coherent-state protocol (i.e.,  $\mu_s = 1$ ). The red lines are the projections of the values of the secret key rate at  $z = 10$  m. Note that the squeezed variance is optimal for each transmission distance and depth.

generality, we define  $X$  quadrature as observables. Thus, the generated squeezed quadratures  $x_s$  and  $p_s$  can be described by the diagonal covariance matrix  $\gamma = \text{diag}(\mu_s, 1/\mu_s)$  with the squeezed variance  $\mu_s$ . Note that we consider ideal squeezed states in the following, regardless of the so-called antisqueezing quadrature noise from the OPO sources. The analysis of antisqueezing noise was well studied in [58].

*Step 2: Displacement.* Alice applies Gaussian quadrature displacement  $x_a$  (zero mean and variance  $\mu_a$ ) on the squeezed states in phase space. Thus, the observable quadratures evolve to  $X$  quadratures  $x_s + x_a$  with variance  $\mu_s + \mu_a$ , while the variance of  $P$  quadratures  $p_s$  remains  $1/\mu_s$ . Correspondingly, the covariance matrix becomes  $\gamma' = \text{diag}(\mu_s + \mu_a, 1/\mu_s)$ .

*Step 3: Transmission and measurement.* The prepared quantum states are transferred to trusted Bob via the fading channel and then measured by coherent detection (homodyne or heterodyne). For a convenient evaluation, we divide the fading channel into  $n$  stable subchannels with constant transmittance  $\{\eta_i\}_{i=1,\dots,n}$  ( $0 \leq \eta_i \leq 1$ ) and corresponding probability  $\{p_i\}_{i=1,\dots,n}$  (so that  $\sum_{i=1}^n p_i = 1$ ) [51]. For the  $i$ th subchannel, the evolution of  $X$  quadratures can be described in the Heisenberg picture, which is given by

$$x_b = \sqrt{\eta_i}(x_s + x_a + x_\epsilon) + \sqrt{1 - \eta_i}x_0, \quad (26)$$

where  $x_0$  is referred to as a shot-noise unit and  $x_\epsilon$  is the excess noise of the channel with variance  $\epsilon$ . Thus, the variance of the  $X$ -quadrature measurement data becomes  $\mu_b^i = 1 + \eta_i(\mu_s + \mu_a - 1 + \epsilon)$ . The overall quantum state of arriving is the mixture of the results in each subchannel weighted by the corresponding probability.

*Step 4: Data processing.* With the aid of classical processing (error correction and privacy amplification [59]), Alice shares a sequence of secure bits with Bob. In this work, we consider the reverse reconciliation scheme since it is more robust against channel attenuation than direct reconciliation [60].

### B. Asymptotic analysis

Next we perform the security analysis of the protocol. We first verify the security of the protocol against the optimal

Gaussian collective attack [61] by calculating the lower bound on the asymptotic key rate  $\mathcal{K}^\infty$ . The eavesdropper Eve is assumed to be capable of purifying all the noise added in the untrusted quantum channel. In terms of the extension of the classical Csiszár-Körner theorem [62], the secure key can be distilled if Alice and Bob have an information advantage over Eve. Therefore, the asymptotic key rate is given by

$$\mathcal{K}^\infty(\mu_s, \mu_a, \langle \eta \rangle, \langle \sqrt{\eta} \rangle, \epsilon) = \beta I_{AB} - \chi_{BE}, \quad (27)$$

where  $\beta$  denotes the reconciliation efficiency,  $I_{AB}$  is the Shannon mutual information between Alice and Bob, and  $\chi_{BE}$  is the Holevo bound, representing the maximum information Eve has stolen. The variance  $\epsilon$  (i.e., excess noise) is related to the background photons  $\mathcal{N}_{\text{back}}$  given by  $\epsilon = 2\mathcal{N}_{\text{back}}/\eta$  [4]. The details of  $I_{AB}$  and  $\chi_{BE}$  are given in Appendix D, where the analysis is established using an equivalent entanglement-based scheme with independent control of squeezing and modulation.

In Fig. 8 we show the asymptotic key rate  $\mathcal{K}^\infty$  of the squeezed-state protocol as a function of transmission distance  $z$  and the depth  $d$  for two types of oceans. The squeezed variance  $\mu_s$  is optimal for each transmission distance and depth. The gray surface, denoting the secret key rates achievable in the coherent-state protocol (i.e.,  $\mu_s = 1$ ), is plotted for comparison. We find that the proposed protocol outperforms the coherent-state protocol in terms of both secret key rate and transmission distance. Looking at the S1 ocean as an example [see Fig. 8(a)], the maximal transmission distance of the squeezed-state protocol, appearing at a depth of 200 m, can reach up to 40 m, whereas the coherent-state protocol loses security once the transmission distance exceeds 34 m (at all depths). Moreover, the secret key rates show a trough when the depth is between 100 and 130 m. This result can be attributed to the specific distribution of the extinction coefficient, as depicted in Fig. 1. Hence, the system should avoid depths of 100–130 m in the S1 ocean. In addition, the communication is insecure at the first 20 m under the ocean surface for both protocols due to the influence of the background photons (see Fig. 5). Note that the coherent-state protocol is unable to provide secret keys even when the depth is increased to 50 m. Similarly, both the coherent-state protocol and the

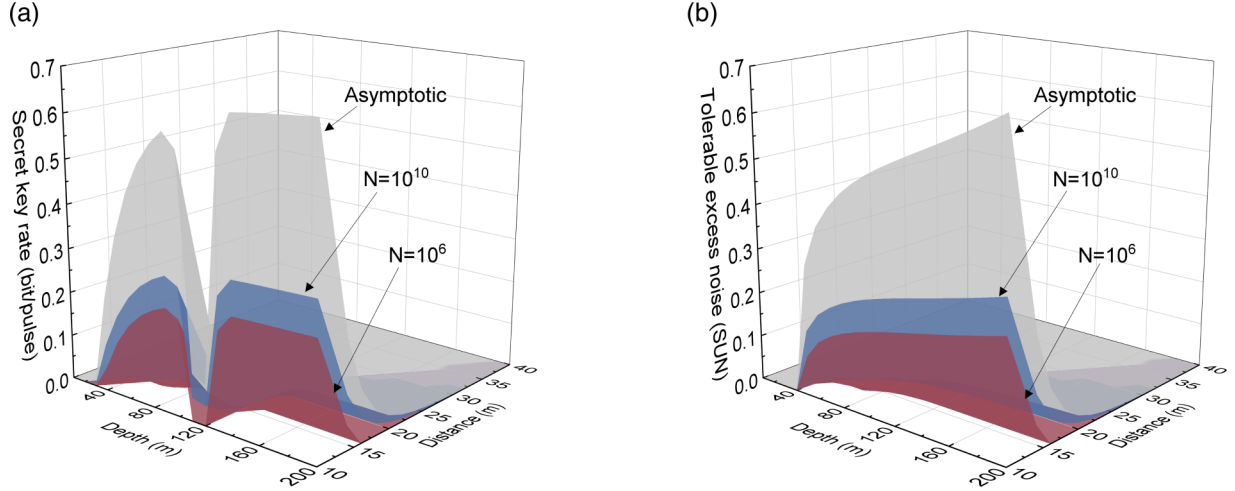


FIG. 9. Finite-size secret key rates of the squeezed-state protocol over two types of ocean: (a) the S1 ocean and (b) the S6 ocean. From top to bottom, the block length  $N$  is equal to  $\infty$ ,  $10^{10}$ , and  $10^6$ .

squeezed-state protocol fail to maintain security in the S6 ocean when the depth is less than 40 m, as shown in Fig. 8(b).

Furthermore, higher levels of squeezing are more advantageous for the ocean-based protocol in terms of optimization results, i.e.,  $\mu_s = 0.1$  is the optimal squeezed variance. In general, the optimal squeezed variance of a fading channel is related to the strength of transmittance fluctuations or, equivalently, the value of  $\text{Var}(\sqrt{\eta})$  [63]. The larger the squeezed variance is, the more sensitive the protocol is to transmittance fluctuation. The relationship between  $\text{Var}(\sqrt{\eta})$  and optimal squeezed variance is shown in Appendix E. We find that stronger squeezing benefits the proposed protocol since the  $\text{Var}(\sqrt{\eta})$  of both the S1 ocean and the S6 ocean are all less than  $10^{-3}$  (see Fig. 3). Moreover, one can further improve the secret key rate by the optimal modulation variance  $\mu_a$ , as shown in Appendix F.

### C. Finite-size regime

In the asymptotic case, the secure analysis is carried out under the assumption that the data length is infinite, which is impossible in practice. Therefore, considering the finite-size effect in security analysis is necessary [4,64]. In the finite-size regime, we need to estimate the unknown parameters, including the channel transmittance and noise. In practice, these parameters are estimated using finite-size data samples so that the secret key rate will be reduced. Although the finite-size effect in fiber links has broadened, the analysis in free space is still a subject to be explored because the channel fluctuation has a negative impact on the parameter estimation [65]. To compensate for imprecise estimation, a suppression method, clustering overall data into small and low-fluctuation blocks, has been proposed [4,66]. However, this method increases the difficulty of the software and hardware at the receiver.

In what follows, we consider the situation in which all data are included within a single signal block. In this situation, the fading channel can be equivalent to a nonfading one with effective transmittance

$$\eta_{\text{eff}} = \langle \sqrt{\eta} \rangle^2 \quad (28)$$

and an extra noise

$$\epsilon_{\text{fad}} = \text{Var}(\sqrt{\eta})(\mu_s + \mu_a - 1). \quad (29)$$

Then Alice and Bob's data follow the linear relation

$$y = tx + \zeta, \quad (30)$$

where  $t = \sqrt{\eta_{\text{eff}}}$  and  $\zeta$  is the total noise term following a Gaussian distribution with variance  $\sigma^2$ . The secret key rate with finite-size effect can be equivalently parametrized as originating from the fixed effective transmittance, which is given by

$$\mathcal{K} = \Lambda [\mathcal{K}^\infty(t_{\min}, \sigma_{\max}^2) - \Delta], \quad (31)$$

where  $\Lambda$  is the proportion of data used for secret key rate generation and  $\Delta$  is related to the security of the privacy amplification given by

$$\Delta = 7\sqrt{\frac{\log_2(2/\bar{\epsilon})}{\Lambda N}} + \frac{2}{\Lambda N} \log_2(1/\epsilon_{\text{PA}}), \quad (32)$$

where  $N$  is the block length,  $\bar{\epsilon}$  is the smoothing parameter, and  $\epsilon_{\text{PA}}$  is the failure probability of the privacy amplification procedure. The values of  $t_{\min}$  and  $\sigma_{\max}^2$  are calculated by the maximum-likelihood estimators

$$\hat{t} = \frac{\sum_{i=1}^{N(1-\Lambda)} x_i y_i}{\sum_{i=1}^{N(1-\Lambda)} x_i^2} \quad (33)$$

and

$$\hat{\sigma}^2 = \frac{1}{N(1-\Lambda)} \sum_{i=1}^{N(1-\Lambda)} (y_i - \hat{t}x_i)^2. \quad (34)$$

Then  $t_{\min}$  and  $\sigma_{\max}^2$  have the results [64]

$$t_{\min} \approx \hat{t} - Z_{\epsilon_{\text{PE}}/2} \sqrt{\frac{\hat{\sigma}^2}{N(1-\Lambda)(\mu_s + \mu_a - 1)}}, \quad (35)$$

$$\sigma_{\max}^2 \approx \hat{\sigma}^2 + Z_{\epsilon_{\text{PE}}/2} \frac{\hat{\sigma}^2 \sqrt{2}}{\sqrt{N(1-\Lambda)}}, \quad (36)$$

where  $\mathcal{Z}_{\epsilon_{\text{PE}}/2} = \sqrt{2}\text{erf}^{-1}(1 - \epsilon_{\text{PE}})$  with the failing probability of parameter estimation  $\epsilon_{\text{PE}}$  and inverse error function  $\text{erf}^{-1}$ .

Figure 9 depicts the finite-size secret key rates  $\mathcal{K}$  vs transmission distance  $z$  and the depth  $d$  for two types of oceans. The parameters  $\bar{\epsilon}$ ,  $\epsilon_{\text{PE}}$ , and  $\epsilon_{\text{PA}}$  are all set to  $10^{-10}$  [64] and half of the signals are used for parameter estimation, i.e.,  $\Lambda = 0.5$ . We find that the finite-size effect is more pronounced if fewer signals are exchanged. When the block length is set to  $10^6$ , the protocol performs significantly worse than when  $N = 10^{10}$ . In general, at least  $10^7$  samples are required under the consideration of Gaussian collective attacks [2]. As the block length grows, more signals can be used for parameter estimation and key extraction, and the secret key rate approaches the asymptotic case. Note that we can optimize the proportion  $\Lambda$  to further improve the secret key rate with  $N$  total samples [67].

## VII. CONCLUSION

We have established the ultimate limits for ocean quantum communications. To describe the evolution of the quantum state, we proposed an analytical method of ocean quantum links, based on the elliptic deformation assumption, for deriving the PDT function for various depths and ocean types. The proposed model shows the effect of seawater on quantum light transmission, with a focus on absorption, scattering, turbulence, and the ocean thermal noise caused by background light. With the aid of PDT, we first derived the pure-loss bound, i.e., PLOB bound, and then extended the results to the case under thermal noise, including a thermal upper bound and a thermal lower bound. In addition, the security of quantum squeezed-state communication protocols was analyzed with squeezed variance optimization. We showed the performance of the system in terms of the secret key rate under a Gaussian collective attack in both the asymptotic case and finite-size regimes.

## ACKNOWLEDGMENTS

We would like to thank Dr. D. Vasylyev and Qingquan Peng for helpful discussions. This work was supported by the National Natural Science Foundation of China (Grant No. 61871407) and Natural Science Foundation of Hunan Province, China (Grant No. 2021JJ30878).

## APPENDIX A: $\mathcal{T}_{\text{abs}}$ AND $\mathcal{T}_{\text{sca}}$ IN EQ. (2)

Mathematically,  $\mathcal{T}_{\text{abs}}$  has the form

$$\mathcal{T}_{\text{abs}} = a_f^0 c_f(d) \exp(-k_f \lambda) + a_h^0 c_h(d) \exp(-k_h \lambda) + a_w + a_c^0 [c_c(d)/c_c^0]^{0.602}, \quad (\text{A1})$$

where  $c_c^0 = 1 \text{ mg/m}^3$ ,  $a_w$  represents the absorption due to pure water in relation to wavelength  $\lambda$  (see Ref. [68]),  $a_f^0 = 35.959 \text{ m}^2/\text{mg}$  is the absorption coefficient of fulvic acid,  $a_h^0 = 18.828 \text{ m}^2/\text{mg}$  is the absorption coefficient of humic acid, and  $k_f = 0.0189 \text{ nm}^{-1}$  and  $k_h = 0.01105 \text{ nm}^{-1}$  are the exponential coefficient of fulvic acid and humic acid, respectively. The concentration of fulvic acid at depth  $d$  is given by

$$c_f(d) = 1.74098 c_c(d) \exp[0.12327 c_c(d)] \quad (\text{A2})$$

and the concentration of humic acid has the form

$$c_h(d) = 0.19334 c_c(d) \exp[0.12343 c_c(d)], \quad (\text{A3})$$

where the concentration of chlorophyll  $a$ ,  $c_c(d)$ , is defined as in Eq. (3). Here  $a_c^0$  denotes the absorption coefficient of chlorophyll  $a$  in relation to  $\lambda$  (see Ref. [69]).

The scattering factor  $\mathcal{T}_{\text{sca}}$  has the form

$$\mathcal{T}_{\text{sca}} = b_w + b_s^0 c_s(d) + b_l^0 c_l(d), \quad (\text{A4})$$

where  $b_w = 0.005826(400/\lambda)^{4.322}$  is the pure water scattering coefficient,  $b_s^0 = 1.1513(400/\lambda)^{1.7}$  is the scattering coefficient of small particulate matter, and  $b_l^0 = 0.3411(400/\lambda)^{0.3}$  is the scattering coefficient of large particulate matter. The parameters  $c_s(d)$  and  $c_l(d)$  are the concentrations of small particles and large particles, respectively, and have the forms

$$c_s(d) = 0.01739 c_c(d) \exp[0.11631 c_c(d)], \quad (\text{A5})$$

$$c_l(d) = 0.76284 c_c(d) \exp[0.03092 c_c(d)]. \quad (\text{A6})$$

## APPENDIX B: DERIVATION OF $\mathcal{M}$ AND $\mathcal{C}$

For a Gaussian beam, the beam amplitude has the form [35]

$$u(\mathbf{r}, z = 0) = \sqrt{\frac{2}{\pi w_0^2}} \exp\left[-\frac{1}{w_0^2} |\mathbf{r}|^2 - \frac{ik}{2f_0} |\mathbf{r}|^2\right], \quad (\text{B1})$$

where  $w_0$  is the initial beam radius,  $\mathbf{r} = (x, y)^T$  is the vector of transverse coordinates,  $k = 2\pi/\lambda$  is the wave number,  $z$  denotes the distance from the transmitter plane, and  $f_0$  is the wave-front radius. In the propagation path, the beam amplitude  $u(\mathbf{r}, z)$  satisfies the paraxial approximation equation given by [35]

$$2ik \frac{\partial u(\mathbf{r}, z)}{\partial z} + \Delta_{\mathbf{r}} u(\mathbf{r}, z) + 2k^2 \delta_n(\mathbf{r}, z) u(\mathbf{r}, z) = 0, \quad (\text{B2})$$

where  $\delta_n(\mathbf{r}, z)$  is a small fluctuating part of the index of air refraction. As for the arriving elliptic beam, its properties can be expressed in terms of the second-order field correlation function [34]

$$\Gamma_2 = \langle u^*(\mathbf{r}, z) u(\mathbf{r}, z) \rangle, \quad (\text{B3})$$

together with the fourth-order field correlation function

$$\Gamma_4 = \langle u^*(\mathbf{r}_1, z) u(\mathbf{r}_1, z) u^*(\mathbf{r}_2, z) u(\mathbf{r}_2, z) \rangle. \quad (\text{B4})$$

With the support of  $\Gamma_2$  and  $\Gamma_4$ , the variance of beam centroid position in  $\mathcal{M}$  [cf. Eq. (13)] can be expressed as

$$\langle \Delta x_0^2 \rangle = \langle \Delta y_0^2 \rangle = \int_{\mathbb{R}^4} d^2 \mathbf{r}_1 d^2 \mathbf{r}_2 x_1 x_2 \Gamma_4 \quad (\text{B5})$$

and the mean and covariance of the squared ellipse semiaxis has the forms

$$\langle \Delta w_i^2 \rangle = 4 \left[ \int_{\mathbb{R}^2} d^2 \mathbf{r} x^2 \Gamma_2 - \langle x_0^2 \rangle \right], \quad (\text{B6})$$

$$\langle \Delta w_i^2 \Delta w_j^2 \rangle = 8 \int_{\mathbb{R}^4} d^2 \mathbf{r}_1 d^2 \mathbf{r}_2 \Gamma_2 [x_1^2 x_2^2 (4\delta_{ij} - 1)]$$

$$\begin{aligned}
& -x_1^2 y_2^2 (4\delta_{ij} - 3)] - 16 \left( \int_{\mathbb{R}^2} d^2 \mathbf{r} x^2 \Gamma_2 \right)^2 \\
& - 16 [4\delta_{ij} - 1] \langle x_0^2 \rangle^2. \quad (\text{B7})
\end{aligned}$$

To acquire  $\Gamma_2$  and  $\Gamma_4$ , we need to solve the paraxial approximation equation as shown in Eq. (B2) to get  $u(\mathbf{r}, z)$ . Based on the Huygens-Kirchhoff method [43], the solution can be expressed as

$$\begin{aligned}
u(\mathbf{r}, z) &= \int_{\mathbb{R}^2} d^2 \mathbf{r}' u(\mathbf{r}', z=0) \\
&\times \mathcal{G}_0(\mathbf{r}, \mathbf{r}'; L, 0) \exp[i\mathcal{S}(\mathbf{r}, \mathbf{r}'; L, 0)], \quad (\text{B8})
\end{aligned}$$

where  $z = L$  is the transmission distance,  $u(\mathbf{r}', z=0)$  is defined in Eq. (B1), and  $\mathcal{G}_0(\mathbf{r}, \mathbf{r}'; L, 0)$  is given by

$$\mathcal{G}_0(\mathbf{r}, \mathbf{r}'; L, 0) = -\frac{ik}{2\pi L} \exp\left(\frac{ik|\mathbf{r} - \mathbf{r}'|^2}{2L}\right). \quad (\text{B9})$$

In addition,  $\mathcal{S}(\mathbf{r}, \mathbf{r}'; L, 0)$  denotes the phase contribution from the fluctuation of the index of ocean refraction over the propagation path, which has the form

$$\mathcal{S}(\mathbf{r}, \mathbf{r}'; L, 0) = k \int_0^L d\xi \delta\left(\mathbf{r} \frac{\xi}{L} + \mathbf{r}' \frac{L-\xi}{L}, \xi\right). \quad (\text{B10})$$

We find that the key step for  $u(\mathbf{r}, z)$  is to derive the phase fluctuation  $\mathcal{S}(\mathbf{r}, \mathbf{r}'; L, 0)$ . In the following derivation, we use the specific form of correlation function, called structure function, for phase fluctuation

$$\mathcal{D}_s(\mathbf{r}_1 - \mathbf{r}_2, \mathbf{r}'_1 - \mathbf{r}'_2) = \langle [\mathcal{S}(\mathbf{r}_1, \mathbf{r}'_1; L, 0) - \mathcal{S}(\mathbf{r}_2, \mathbf{r}'_2; L, 0)]^2 \rangle. \quad (\text{B11})$$

The structure function can be acquired by combining Eq. (B10), Eq. (B11), and the ocean power spectrum in Eq. (8). For a detailed derivation of Eq. (B11) refer to the Supplemental Material of Ref. [21]. In the derivation, we use two types of Gaussian integrals, which have the forms

$$\int_{-\infty}^{\infty} dx \exp(Ax^2 + jBx), \quad (\text{B12})$$

$$\int_{-\infty}^{\infty} dx x^2 \exp(Ax^2 + jBx), \quad (\text{B13})$$

where  $j^2 = -1$ . Finally, the last two parameters of  $\mathcal{M}$  can be calculated as

$$\langle \Delta x_0^2 \rangle = \langle \Delta y_0^2 \rangle = 27.12 \omega^{4/5} \xi^{-4/15} k^{-1/15} z^{37/15} \quad (\text{B14})$$

and the elements of  $\mathcal{C}$  have the forms

$$\langle \Theta_i \rangle = \ln \left( \frac{[a_1 \mathcal{F}_1^3 - a_2 \mathcal{F}_1^2 + \Omega + \Omega^{-1}]^2}{\sqrt{[1 + \Omega^2 + (a_1 \mathcal{F}_1 - a_2) \mathcal{F}_1^2 \Omega]^2 + a_3 \mathcal{F}_2}} \right), \quad (\text{B15})$$

$$\langle \Delta \Theta_i^2 \rangle = \ln \left( 1 + \frac{a_4 \mathcal{F}_2}{[1 + \Omega^2 + (a_1 \mathcal{F}_1 - a_2) \mathcal{F}_1^2 \Omega]^2} \right), \quad (\text{B16})$$

$$\langle \Delta \Theta_1 \Delta \Theta_2 \rangle = \ln \left( 1 + \frac{a_5 \mathcal{F}_2 \Omega^{-2}}{[a_1 \mathcal{F}_1^3 - a_2 \mathcal{F}_1^2 + \Omega + \Omega^{-1}]^2} \right), \quad (\text{B17})$$

where  $a_1 = 131.4$ ,  $a_2 = 54.06$ ,  $a_3 = 248.99$ ,  $a_4 = 1009.81$ ,  $a_5 = 49.95$ ,  $\Omega = kw_0^2/2z$  is the Fresnel parameter,  $\mathcal{F}_1 := \omega^{2/5} \xi^{-2/15} k^{7/15} z^{11/15}$ , and  $\mathcal{F}_2 := \omega^{6/5} \xi^{-2/5} k^{7/5} z^{11/5} (1 + \Omega^2) \Omega$ . Note that  $\Theta_i = \ln(w_i^2/w_0^2)$  with ellipse semiaxes  $w_i$ .

### APPENDIX C: MONTE CARLO METHOD OF THE ELLIPTIC-BEAM MODEL IN THE OCEAN TURBULENCE CHANNEL

Following the elements above, the transmittance  $\eta$  in the Monte Carlo method can be estimated by

$$\eta = \eta_{\text{ext}} \eta_0 \exp \left\{ - \left[ \frac{r/a}{\mathcal{Q}\left(\frac{2}{w_{\text{eff}}(\phi-\varphi)}\right)} \right]^{\mathcal{Y}[2/w_{\text{eff}}(\phi-\varphi)]} \right\}, \quad (\text{C1})$$

where the extinction-induced transmittance  $\eta_{\text{ext}}$  is defined as in Eq. (1),  $a$  is the receiver telescope radius,  $r = (x_0, y_0)$  is the beam-centroid vector (see Fig. 2),  $\phi$  is the beam-ellipse orientation angle,  $\varphi$  is the angle between vector  $r$  and  $x$  axis, and  $\eta_0$  denotes the transmittance without both extinction and beam wandering effects, which can be expressed as

$$\begin{aligned}
\eta_0 &= 1 - I_0 \left( a^2 \left[ \frac{1}{w_1^2} - \frac{1}{w_2^2} \right] \right) \exp \left[ -a^2 \left( \frac{1}{w_1^2} + \frac{1}{w_2^2} \right) \right] \\
&- 2 \left\{ 1 - \exp \left[ -\frac{a^2}{2} \left( \frac{1}{w_1} - \frac{1}{w_2} \right)^2 \right] \right\} \\
&\times \exp \left\{ - \left[ \frac{(w_1+w_2)^2}{|w_1^2-w_2^2|} \right]^{\mathcal{Y}(1/w_1-1/w_2)} \right\}, \quad (\text{C2})
\end{aligned}$$

where  $w_1$  and  $w_2$  are ellipse semiaxes and  $\mathcal{Q}(\cdot)$  and  $\mathcal{Y}(\cdot)$  are scale and shape functions, respectively. The two functions have the forms

$$\mathcal{Q}(x) = \left[ \ln \left( 2 \frac{1 - \exp[-\frac{1}{2}a^2x^2]}{1 - \exp[-a^2x^2]I_0(a^2x^2)} \right) \right]^{-1/\mathcal{Y}(x)}, \quad (\text{C3})$$

$$\begin{aligned}
\mathcal{Y}(x) &= 2a^2x^2 \frac{\exp(-a^2x^2)I_1(a^2x^2)}{1 - \exp(-a^2x^2)I_0(a^2x^2)} \\
&\times \left[ \ln \left( 2 \frac{1 - \exp[-\frac{1}{2}a^2x^2]}{1 - \exp[-a^2x^2]I_0(a^2x^2)} \right) \right]^{-1}, \quad (\text{C4})
\end{aligned}$$

where  $I_i(\cdot)$  is the modified Bessel function of the  $i$ th order. In Eq. (C1)  $w_{\text{eff}}(\cdot)$  is the effective spot radius with deformation effects given by

$$\begin{aligned}
w_{\text{eff}}(x) &= 2a \left[ \mathcal{W} \left( \frac{4a^2}{w_1 w_2} \exp \left( \frac{a^2[1 + 2\cos^2(x)]}{w_1^2} \right) \right. \right. \\
&\left. \left. + \frac{a^2[1 + 2\sin^2(x)]}{w_2^2} \right) \right]^{-1/2}, \quad (\text{C5})
\end{aligned}$$

where  $\mathcal{W}(\cdot)$  denotes the Lambert  $W$  function.

### APPENDIX D: CALCULATION OF SECRET KEY RATE

The secret key rate in the asymptotic case is shown in Eq. (27). The classical mutual information  $I_{\text{AB}}$  can be obtained

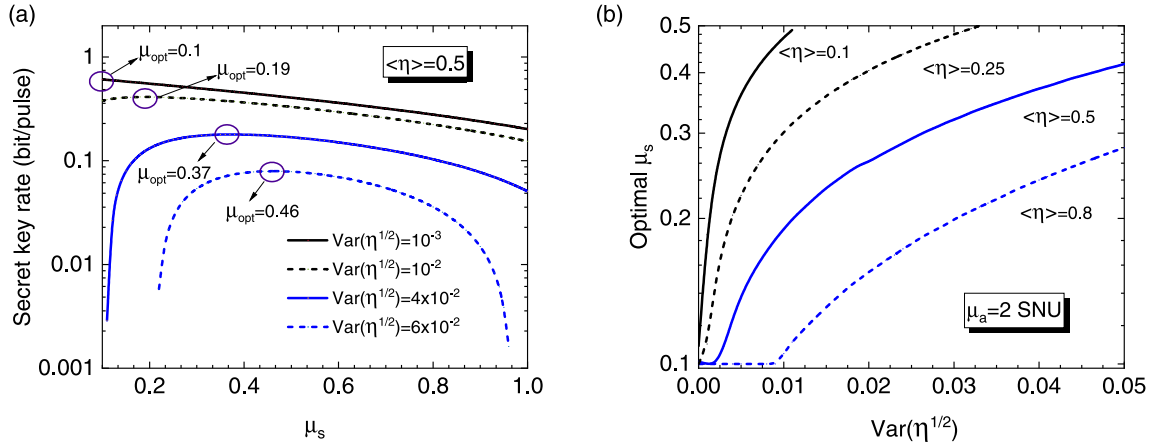


FIG. 10. (a) Secret key rate vs squeezed variance with various  $\text{Var}(\sqrt{\eta})$ . Here  $\mu_{\text{opt}}$  denotes the optimal squeezed variance. The mean transmittance is set to 0.5. (b) Optimal squeezed variance vs transmittance fluctuations under different mean transmittance. Refer to Table II for the simulation parameters.

from the variances and the correlations between the modulation data and measurement data and is given by

$$I_{AB} = \frac{1}{2} \log \frac{\mu_a}{\mu_{a|b}}, \quad (\text{D1})$$

where  $\mu_a$  is the modulation variance,  $\mu_{a|b} = \mu_a - c_{ab}^2/\mu_b$  is the conditional variance with the correlation  $c_{ab}^2$ , and  $\mu_b$  is the variance of measured data. As mentioned below Eq. (26), the variance of measured data in the  $i$ th subchannel has the form  $\mu_b^i = 1 + \eta_i(\mu_s + \mu_a - 1 + \epsilon)$ . Then the value of  $I_{AB}$  in the  $i$ th subchannel is given by

$$I_{AB}^i = \frac{1}{2} \log_2 \left[ 1 + \frac{\eta_i \mu_a}{1 + \eta_i(\mu_s + \epsilon - 1)} \right] \quad (\text{D2})$$

and the overall mutual information in the fluctuating channel has the form

$$I_{AB} = \frac{1}{2} \log_2 \left[ 1 + \frac{\langle \sqrt{\eta} \rangle^2 \mu_a}{1 + \langle \eta \rangle (\mu_s + \mu_a + \epsilon - 1) - \langle \sqrt{\eta} \rangle^2 \mu_a} \right]. \quad (\text{D3})$$

In addition, the Holevo bound  $\chi_{BE}$  for reverse reconciliation is identified as [70]

$$\chi_{BE} = g\left(\frac{\mathcal{V}_1 - 1}{2}\right) + g\left(\frac{\mathcal{V}_2 - 1}{2}\right) - g\left(\frac{\mathcal{V}_3 - 1}{2}\right), \quad (\text{D4})$$

where  $g(x) := (x + 1) \log_2(x + 1) - x \log_2 x$  and  $\mathcal{V}_{1,2,3}$  are the symplectic eigenvalues derived from the covariance matrices of the sharing quantum state. Here we use the equivalent entanglement-based scheme instead of the prepare-and-measure scheme in Fig. 7 for security analysis and characterize the quantum state by a two-mode covariance matrix [71]. The overall covariance matrix over the fluctuating channel is the weighted average of the matrices in each subchannel [51]. The symplectic eigenvalues  $\mathcal{V}_{1,2}$  can be derived from the overall covariance matrix, which has the form

$$\mathcal{U}_{AB} = \begin{bmatrix} \tilde{A} \mathbf{I} & \tilde{C} \mathbf{R} \\ \tilde{C} \mathbf{R} & \tilde{B} \mathbf{I} \end{bmatrix}, \quad (\text{D5})$$

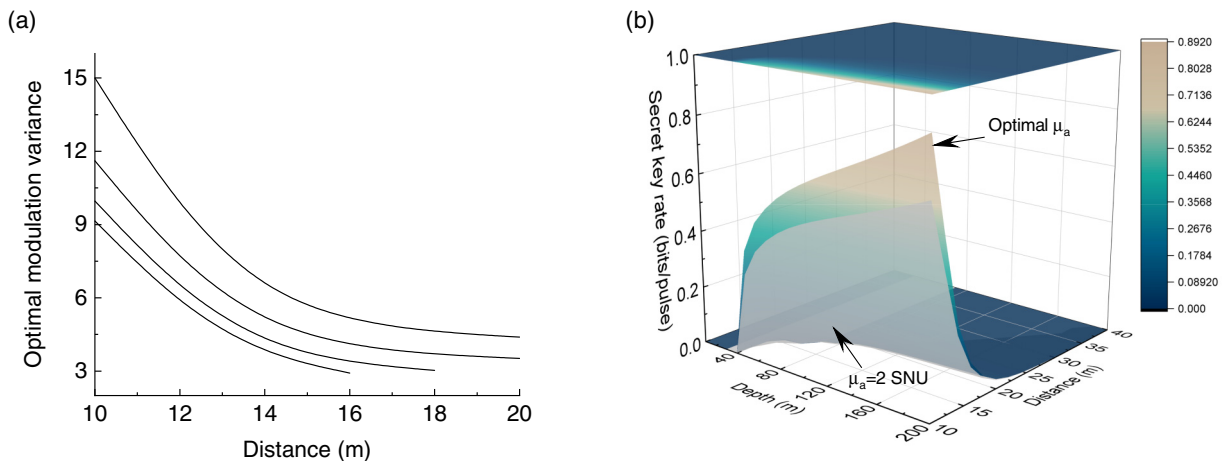


FIG. 11. (a) Optimal modulation variance versus transmission distance. From top to bottom, the squeezed variance is equal to 0.1, 0.5, 0.8, and 1. (b) Secret key rate with optimal modulation variance. The gray surface represents a secret key rate of  $\mu_a = 2$  SNU.

where  $\mathbf{I} = \text{diag}(1, 1)$  and  $\mathbf{R} = \text{diag}(1, -1)$ . The submatrices are given by

$$\tilde{A} = \begin{bmatrix} \mu_s + \mu_a & 0 \\ 0 & \frac{1}{\mu_s} \end{bmatrix}, \quad (\text{D6})$$

$$\tilde{B} = \begin{bmatrix} 1 + \langle \eta \rangle (\mu_s + \mu_a - 1 + \epsilon) & 0 \\ 0 & 1 + \frac{\langle \eta \rangle (1 - \mu_s + \mu_s \epsilon)}{\mu_s} \end{bmatrix}, \quad (\text{D7})$$

$$\tilde{C} = \begin{bmatrix} \langle \sqrt{\eta} \rangle \sqrt{\mu_a (\mu_s + \mu_a)} & 0 \\ 0 & \frac{\langle \sqrt{\eta} \rangle \mu_a}{\mu_s \sqrt{\mu_a (\mu_s + \mu_a)}} \end{bmatrix}. \quad (\text{D8})$$

Another symplectic eigenvalue  $\mathcal{V}_3$  is derived from the covariance matrix  $\mathcal{U}_A^{x_b}$  after Bob's homodyne measurement in  $X$  quadratures. Specifically, the homodyne measurement gives [72]

$$\mathcal{U}_A^{x_b} = \mathcal{U}_A - \sigma_{AB} (\mathcal{X} \mathcal{U}_B \mathcal{X})^{\text{MP}} \sigma_{AB}^T, \quad (\text{D9})$$

where  $\mathcal{U}_A$ ,  $\mathcal{U}_B$ , and  $\sigma_{AB}$  are the submatrices of  $\mathcal{U}_{AB}$ ,  $\mathcal{X} = \text{diag}(1, 0)$ , and MP denotes the inverse on the range. Therefore,  $\mathcal{U}_A^{x_b}$  is given by

$$\mathcal{U}_A^{x_b} = \begin{bmatrix} \frac{(\mu_s + \mu_a)[1 - \langle \sqrt{\eta} \rangle^2 \mu_a + \langle \eta \rangle (\mu_s + \mu_a - 1 + \epsilon)]}{1 + \langle \eta \rangle (\mu_s + \mu_a - 1 + \epsilon)} & 0 \\ 0 & \frac{1}{\mu_s} \end{bmatrix}. \quad (\text{D10})$$

## APPENDIX E: RELATIONSHIP BETWEEN $\text{Var}(\sqrt{\eta})$ AND OPTIMAL SQUEEZED VARIANCE

The asymptotic key rate  $\mathcal{K}^\infty$  as a function of the squeezed variance  $\mu_s$  for different  $\text{Var}(\sqrt{\eta})$  is shown in Fig. 10(a). Here we consider the case without both background noise and excess noise. We find that the squeezed variance should be optimized to achieve the best performance in terms of  $\text{Var}(\sqrt{\eta})$ . In Fig. 10(b) we plot the relationship between the optimal  $\mu_s$  and  $\text{Var}(\sqrt{\eta})$  for different mean transmittance  $\langle \eta \rangle$ . We find that smaller squeezed variance is always more beneficial for a nonfluctuation channel. As fluctuation increases, the optimal squeezed variance is shifted towards larger values, corresponding to weaker squeezing.

## APPENDIX F: OPTIMIZATION OF MODULATION VARIANCE

In Fig. 11 the influence of the modulation variance  $\mu_a$  on the squeezed-state protocol is studied. Figure 11(a) shows the optimal modulation variance  $\mu_{\text{opt}}$  as a function of transmission distance  $z$  for various squeezed variance  $\mu_s$ . Here we present the results of the S6 ocean at a depth of  $d = 200$  m as an example. Weakly, moderately, and strongly squeezed states correspond to  $\mu_s = 0.1, 0.5, \text{ and } 0.8$ , respectively [73]. We find that the optimal modulation variance shows a downward trend with the increasing distance. In addition, as the squeezed variance goes up, the optimal modulation variance at a specific transmission distance will be decreased. Figure 11(b) shows the secret key rate of the proposed protocol with optimal  $\mu_a$ . We find that the modulation variance should be adjusted for a higher secret key rate after the squeezed variance is determined.

- 
- [1] N. Gisin, G. Ribordy, W. Tittel, and H. Zbinden, Quantum cryptography, *Rev. Mod. Phys.* **74**, 145 (2002).
- [2] S. Pirandola, U. L. Andersen, L. Banchi, M. Berta, D. Bunandar, R. Colbeck, D. Englund, T. Gehring, C. Lupo, C. Ottaviani *et al.*, Advances in quantum cryptography, *Adv. Opt. Photon.* **12**, 1012 (2020).
- [3] T. Schmitt-Manderbach, H. Weier, M. Fürst, R. Ursin, F. Tiefenbacher, T. Scheidl, J. Perdigues, Z. Sodnik, C. Kurtsiefer, J. G. Rarity *et al.*, Experimental Demonstration of Free-Space Decoy-State Quantum Key Distribution over 144 km, *Phys. Rev. Lett.* **98**, 010504 (2007).
- [4] S. Pirandola, Limits and security of free-space quantum communications, *Phys. Rev. Research* **3**, 013279 (2021).
- [5] M. Ghalaii and S. Pirandola, Quantum communications in a moderate-to-strong turbulent space, *arXiv:2107.12415*.
- [6] S.-K. Liao, W.-Q. Cai, W.-Y. Liu, L. Zhang, Y. Li, J.-G. Ren, J. Yin, Q. Shen, Y. Cao, Z.-P. Li *et al.*, Satellite-to-ground quantum key distribution, *Nature (London)* **549**, 43 (2017).
- [7] Z. Zuo, Y. Wang, D. Huang, and Y. Guo, Atmospheric effects on satellite-mediated continuous-variable quantum key distribution, *J. Phys. A: Math. Theor.* **53**, 465302 (2020).
- [8] S. Pirandola, Satellite quantum communications: Fundamental bounds and practical security, *Phys. Rev. Research* **3**, 023130 (2021).
- [9] W. Cox and J. Muth, Simulating channel losses in an underwater optical communication system, *J. Opt. Soc. Am. A* **31**, 920 (2014).
- [10] X. Yi and I. B. Djordjevic, Power spectrum of refractive-index fluctuations in turbulent ocean and its effect on optical scintillation, *Opt. Express* **26**, 10188 (2018).
- [11] P. A. Hiskett and R. A. Lamb, Underwater optical communications with a single photon-counting system, *Proc. SPIE* **9114**, 91140P (2014).
- [12] Z. Feng, S. Li, and Z. Xu, Experimental underwater quantum key distribution, *Opt. Express* **29**, 8725 (2021).
- [13] C.-Q. Hu, Z.-Q. Yan, J. Gao, Z.-M. Li, H. Zhou, J.-P. Dou, and X.-M. Jin, Decoy-State Quantum Key Distribution over a Long-Distance High-Loss Air-Water Channel, *Phys. Rev. Appl.* **15**, 024060 (2021).
- [14] F. Hufnagel, A. Sit, F. Bouchard, Y. Zhang, D. England, K. Heshami, B. J. Sussman, and E. Karimi, Investigation of underwater quantum channels in a 30 meter flume tank using structured photons, *New J. Phys.* **22**, 093074 (2020).
- [15] L. Ji, J. Gao, A.-L. Yang, Z. Feng, X.-F. Lin, Z.-G. Li, and X.-M. Jin, Towards quantum communications in free-space seawater, *Opt. Express* **25**, 19795 (2017).

- [16] F. Hufnagel, A. Sit, F. Grenapin, F. Bouchard, K. Heshami, D. England, Y. Zhang, B. J. Sussman, R. W. Boyd, G. Leuchs *et al.*, Characterization of an underwater channel for quantum communications in the Ottawa river, *Opt. Express* **27**, 26346 (2019).
- [17] Z. Liu, J. Chen, and D. Zhao, Experimental study of propagation properties of vortex beams in oceanic turbulence, *Appl. Opt.* **56**, 3577 (2017).
- [18] R. J. Glauber, Photon Correlations, *Phys. Rev. Lett.* **10**, 84 (1963).
- [19] V. I. Tatarskii, *The Effects of the Turbulent Atmosphere on Wave Propagation* (Jerusalem: Israel Program for Scientific Translations, Springfield, 1971).
- [20] H. Kaushal and G. Kaddoum, Underwater optical wireless communication, *IEEE Access* **4**, 1518 (2016).
- [21] D. Vasylyev, A. A. Semenov, and W. Vogel, Atmospheric Quantum Channels with Weak and Strong Turbulence, *Phys. Rev. Lett.* **117**, 090501 (2016).
- [22] J. Peřina, V. Peřinová, M. C. Teich, and P. Diamant, Two descriptions for the photocounting detection of radiation passed through a random medium: A comparison for the turbulent atmosphere, *Phys. Rev. A* **7**, 1732 (1973).
- [23] P. Huang and G. Zeng, Entanglement transmission through dense scattering medium, *New J. Phys.* **22**, 053021 (2020).
- [24] J. Gariano and I. B. Djordjevic, Theoretical study of a submarine to submarine quantum key distribution systems, *Opt. Express* **27**, 3055 (2019).
- [25] S. Pirandola, R. Laurenza, C. Ottaviani, and L. Banchi, Fundamental limits of repeaterless quantum communications, *Nat. Commun.* **8**, 15043 (2017).
- [26] R. García-Patrón and N. J. Cerf, Continuous-Variable Quantum Key Distribution Protocols Over Noisy Channels, *Phys. Rev. Lett.* **102**, 130501 (2009).
- [27] Y. Xiang, Y. Wang, X. Ruan, Z. Zuo, and Y. Guo, Improving the discretely modulated underwater continuous-variable quantum key distribution with heralded hybrid linear amplifier, *Phys. Scr.* **96**, 065103 (2021).
- [28] T. Kameda and S. Matsumura, Chlorophyll biomass off Sanriku, northwestern Pacific, estimated by Ocean Color and Temperature Scanner (OCTS) and a vertical distribution model, *J. Oceanogr.* **54**, 509 (1998).
- [29] L. J. Johnson, R. J. Green, and M. S. Leeson, Underwater optical wireless communications: Depth dependent variations in attenuation, *Appl. Opt.* **52**, 7867 (2013).
- [30] Y. Guo, C. Xie, P. Huang, J. Li, L. Zhang, D. Huang, and G. Zeng, Channel-parameter estimation for satellite-to-submarine continuous-variable quantum key distribution, *Phys. Rev. A* **97**, 052326 (2018).
- [31] W. Wang, P. Wang, T. Cao, H. Tian, Y. Zhang, and L. Guo, Performance investigation of underwater wireless optical communication system using  $M$ -ary OAMSK modulation over oceanic turbulence, *IEEE Photon. J.* **9**, 1 (2017).
- [32] N. Jovanovic, C. Schwab, O. Guyon, J. Lozi, N. Cvetojevic, F. Martinache, S. Leon-Saval, B. Norris, S. Gross, D. Doughty *et al.*, Efficient injection from large telescopes into single-mode fibres: Enabling the era of ultra-precision astronomy, *Astron. Astrophys.* **604**, A122 (2017).
- [33] V. V. Nikishov and V. I. Nikishov, Spectrum of turbulent fluctuations of the sea-water refraction index, *Int. J. Fluid Mech. Res.* **27**, 82 (2000).
- [34] L. C. Andrews and R. L. Phillips, *Laser Beam Propagation through Random Media* (SPIE, Bellingham, 2005).
- [35] R. L. Fante, Electromagnetic beam propagation in turbulent media, *Proc. IEEE* **63**, 1669 (1975).
- [36] V. I. Tatarski, *Wave Propagation in a Turbulent Medium* (Courier Dover, Mineola, 2016).
- [37] W. W. Hou, A simple underwater imaging model, *Opt. Lett.* **34**, 2688 (2009).
- [38] G. K. Batchelor, Small-scale variation of convected quantities like temperature in turbulent fluid. Part I. General discussion and the case of small conductivity, *J. Fluid Mech.* **5**, 113 (1959).
- [39] D. Y. Vasylyev, A. A. Semenov, and W. Vogel, Toward Global Quantum Communication: Beam Wandering Preserves Non-classicality, *Phys. Rev. Lett.* **108**, 220501 (2012).
- [40] D. Vasylyev, A. A. Semenov, and W. Vogel, Characterization of free-space quantum channels, *Proc. SPIE* **10771**, 107710V (2018).
- [41] W. Liu, Z. Xu, and L. Yang, SIMO detection schemes for underwater optical wireless communication under turbulence, *Photon. Res.* **3**, 48 (2015).
- [42] Z. Zuo, Y. Wang, Q. Liao, and Y. Guo, Overcoming the uplink limit of satellite-based quantum communication with deterministic quantum teleportation, *Phys. Rev. A* **104**, 022615 (2021).
- [43] V. A. Banakh and V. L. Mironov, Phase approximation of the Huygens-Kirchhoff method in problems of space-limited optical-beam propagation in turbulent atmosphere, *Opt. Lett.* **4**, 259 (1979).
- [44] S.-Y. Shen, M.-W. Dai, X.-T. Zheng, Q.-Y. Sun, G.-C. Guo, and Z.-F. Han, Free-space continuous-variable quantum key distribution of unidimensional Gaussian modulation using polarized coherent states in an urban environment, *Phys. Rev. A* **100**, 012325 (2019).
- [45] Z. Zuo, Y. Wang, Y. Mao, W. Ye, L. Hu, D. Huang, and Y. Guo, Quantum catalysis-assisted attenuation for improving free-space continuous-variable quantum key distribution, *J. Phys. B* **53**, 185501 (2020).
- [46] P. Shi, S.-C. Zhao, Y.-J. Gu, and W.-D. Li, Channel analysis for single photon underwater free space quantum key distribution, *J. Opt. Soc. Am. A* **32**, 349 (2015).
- [47] J. W. Giles and I. N. Bankman, 2005 *IEEE Military Communications Conference* (IEEE, Piscataway, 2005), pp. 1700–1705.
- [48] T. Eberle, V. Händchen, and R. Schnabel, Stable control of 10 dB two-mode squeezed vacuum states of light, *Opt. Express* **21**, 11546 (2013).
- [49] V. Scarani, H. Bechmann-Pasquinucci, N. J. Cerf, M. Dušek, N. Lütkenhaus, and M. Peev, The security of practical quantum key distribution, *Rev. Mod. Phys.* **81**, 1301 (2009).
- [50] V. C. Usenko, I. Derkach, and R. Filip, 2019 *42nd International Conference on Telecommunications and Signal Processing (TSP), Budapest* (IEEE, Piscataway, 2019), pp. 389–392.
- [51] V. C. Usenko, B. Heim, C. Peuntinger, C. Wittmann, C. Marquardt, G. Leuchs, and R. Filip, Entanglement of Gaussian states and the applicability to quantum key distribution over fading channels, *New J. Phys.* **14**, 093048 (2012).
- [52] L. C. Andrews, R. L. Phillips, and C. Y. Hopen, *Laser Beam Scintillation with Applications* (SPIE, Bellingham, 2001), Vol. 99.
- [53] D. Vasylyev, W. Vogel, and F. Moll, Satellite-mediated quantum atmospheric links, *Phys. Rev. A* **99**, 053830 (2019).

- [54] V. Vedral, The role of relative entropy in quantum information theory, *Rev. Mod. Phys.* **74**, 197 (2002).
- [55] S. Jaruwatanadilok, Underwater wireless optical communication channel modeling and performance evaluation using vector radiative transfer theory, *IEEE J. Sel. Areas Commun.* **26**, 1620 (2008).
- [56] S. Q. Duntley, Light in the sea, *J. Opt. Soc. Am.* **53**, 214 (1963).
- [57] S. Pirandola, R. García-Patrón, S. L. Braunstein, and S. Lloyd, Direct and Reverse Secret-Key Capacities of a Quantum Channel, *Phys. Rev. Lett.* **102**, 050503 (2009).
- [58] V. C. Usenko and A. n. Oruganti, *2020 43rd International Conference on Telecommunications and Signal Processing (TSP), Milan* (IEEE, Piscataway, 2020), pp. 421–425.
- [59] A. G. Mountogiannakis, P. Papanastasiou, B. Braverman, and S. Pirandola, Composably-secure data-processing in continuous variable quantum key distribution, [arXiv:2103.16589](https://arxiv.org/abs/2103.16589).
- [60] F. Grosshans, G. V. Assche, J. Wenger, R. Brouri, N. J. Cerf, and P. Grangier, Quantum key distribution using Gaussian-modulated coherent states, *Nature (London)* **421**, 238 (2003).
- [61] M. Navascués, F. Grosshans, and A. Acín, Optimality of Gaussian Attacks in Continuous-Variable Quantum Cryptography, *Phys. Rev. Lett.* **97**, 190502 (2006).
- [62] I. Csiszár and J. Körner, Broadcast channels with confidential messages, *IEEE Trans. Inf. Theory* **24**, 339 (1978).
- [63] I. Derkach, V. C. Usenko, and R. Filip, Squeezing-enhanced quantum key distribution over atmospheric channels, *New J. Phys.* **22**, 053006 (2020).
- [64] A. Leverrier, F. Grosshans, and P. Grangier, Finite-size analysis of a continuous-variable quantum key distribution, *Phys. Rev. A* **81**, 062343 (2010).
- [65] N. Hosseinidehaj, N. Walk, and T. C. Ralph, Composable finite-size effects in free-space continuous-variable quantum-key-distribution systems, *Phys. Rev. A* **103**, 012605 (2021).
- [66] L. Ruppert, C. Peuntinger, B. Heim, K. Günthner, V. C. Usenko, D. Elser, G. Leuchs, R. Filip, and C. Marquardt, Fading channel estimation for free-space continuous-variable secure quantum communication, *New J. Phys.* **21**, 123036 (2019).
- [67] P. Wang, X. Wang, and Y. Li, Continuous-variable measurement-device-independent quantum key distribution using modulated squeezed states and optical amplifiers, *Phys. Rev. A* **99**, 042309 (2019).
- [68] V. I. Haltrin and G. W. Kattawar, Effects of Raman scattering and fluorescence on apparent optical properties of seawater, Texas A&M University report, 1991 (unpublished).
- [69] C. S. Yentsch, The influence of phytoplankton pigments on the colour of sea water, *Deep Sea Res.* **7**, 1 (1960).
- [70] A. S. Holevo and R. F. Werner, Evaluating capacities of bosonic Gaussian channels, *Phys. Rev. A* **63**, 032312 (2001).
- [71] C. Weedbrook, S. Pirandola, R. García-Patrón, N. J. Cerf, T. C. Ralph, J. H. Shapiro, and S. Lloyd, Gaussian quantum information, *Rev. Mod. Phys.* **84**, 621 (2012).
- [72] J. Lodewyck, M. Bloch, R. García-Patrón, S. Fossier, E. Karpov, E. Diamanti, T. Debuisschert, N. J. Cerf, R. Tualle-Brouri, S. W. McLaughlin *et al.*, Quantum key distribution over 25 km with an all-fiber continuous-variable system, *Phys. Rev. A* **76**, 042305 (2007).
- [73] V. C. Usenko and R. Filip, Squeezed-state quantum key distribution upon imperfect reconciliation, *New J. Phys.* **13**, 113007 (2011).